Studying ventricular abnormalities in mild cognitive impairment with hyperbolic Ricci flow and tensor-based morphometry

Jie Shi [a], Cynthia M. Stonnington [b], Paul M. Thompson [c], Kewei Chen [d], Boris Gutman [c], Cole Reschke [d],
Leslie C. Baxter [e], Eric M. Reiman [d], Richard J. Caselli [f], Yalin Wang [a,*],
for the Alzheimer's Disease Neuroimaging Initiative [1]

[a] School of Computing, Informatics, and Decision Systems Engineering, Arizona State University, Tempe, AZ, USA
[b] Department of Psychiatry and Psychology, Mayo Clinic Arizona, Scottsdale, AZ, USA
[c] Imaging Genetics Center, Institute for Neuroimaging and Informatics, University of Southern California, Los Angeles, CA, USA
[d] Banner Alzheimer's Institute and Banner Good Samaritan PET Center, Phoenix, AZ, USA
[e] Human Brain Imaging Laboratory, Barrow Neurological Institute, Phoenix, AZ, USA
[f] Department of Neurology, Mayo Clinic Arizona, Scottsdale, AZ, USA

ARTICLE INFO

ABSTRACT

Mild Cognitive Impairment (MCI) is a transitional stage between normal aging and dementia and people with MCI are at high risk of progression to dementia. MCI is attracting increasing attention, as it offers an opportunity to target the disease process during an early symptomatic stage. Structural magnetic resonance imaging (MRI) measures have been the mainstay of Alzheimer's disease (AD) imaging research, however, ventricular morphometry analysis remains challenging because of its complicated topological structure. Here we describe a novel ventricular morphometry system based on the hyperbolic Ricci flow method and tensor-based morphometry (TBM) statistics. Unlike prior ventricular surface parameterization methods, hyperbolic conformal parameterization is angle-preserving and does not have any singularities. Our system generates a one-to-one diffeomorphic mapping between ventricular surfaces with consistent boundary matching conditions. The TBM statistics encode a great deal of surface deformation information that could be inaccessible or overlooked by other methods. We applied our system to the baseline MRI scans of a set of MCI subjects from the Alzheimer's Disease Neuroimaging Initiative (ADNI: 71 MCI converters vs. 62 MCI stable). Although the combined ventricular area and volume features did not differ between the two groups, our fine-grained surface analysis revealed significant differences in the ventricular regions close to the temporal lobe and posterior cingulate, structures that are affected early in AD. Significant correlations were also detected between ventricular morphometry, neuropsychological measures, and a previously described imaging index based on fluorodeoxyglucose positron emission tomography (FDG-PET) scans. This novel ventricular morphometry method may offer a new and more sensitive approach to study preclinical and early symptomatic stage AD.

© 2014 Elsevier Inc. All rights reserved.

Introduction

Mild Cognitive Impairment (MCI) describes individuals who cognitively lie between normal aging and dementia, and MCI often progresses to Alzheimer's disease (AD). The prevalence of MCI is as high as 19% in persons over age 65, and 29% in those over age 85 (Small et al., 2009). Also, a significant portion of the population diagnosed with life limiting illnesses (LLI) has therapeutic exposures that place them at risk for MCI. As MCI has the greatest risk of progression to dementia, it is a primary focus of interest in aging studies (Roberts et al., 2010). The International Classification of Diseases now has a billing code for MCI (331.83) (ICD, 2010). Over half of those with MCI progress to dementia within 5 years (Gauthier et al., 2006), and early detection of those MCI individuals who will convert to dementia can facilitate earlier intervention, and guide recruitment for clinical trials. Current therapeutic failures in patients with symptomatic memory loss might reflect intervention that is too late, or targets that are secondary effects and less relevant to disease initiation and early progression (Hyman, 2011).

As the paradigm in AD research shifts to a new stage, targeting earlier intervention and prevention (Caselli and Reiman, 2013; Langbaum

---

et al., 2013), there is a requirement for biologically grounded, highly objective biomarkers that can help to identify those high AD risk MCI individuals for whom early intervention may be most appropriate. Various neuroimaging techniques can track disease progression and therapeutic efficacy in MCI (Caroli et al., 2012; Chen et al., 2011; Matsuda, 2007b; Petersen, 2011; Petersen and Jack, 2009; Pihlajamaki et al., 2009; Small et al., 2006; Wolf et al., 2003) and others are beginning to identify abnormal anatomical or functional patterns and their rates of decline. Structural magnetic resonance imaging (MRI) has been the mainstay of AD imaging research and has included evaluations of whole-brain (Chen et al., 2007; Fox et al., 1999; Stonnington et al., 2010), entorhinal cortex (Cardenas et al., 2011), hippocampus (Apostolova et al., 2010b; den Heijer et al., 2010; Jack et al., 2003, 2010; Reiman et al., 1998; Thompson et al., 2004a; Wolz et al., 2010), and temporal lobe volumes (Hua et al., 2010), as well as ventricular enlargement (Jack et al., 2003, 2008; Thompson et al., 2004a; Wang et al., 2011). These correlate closely with differences and changes in cognitive performance, supporting their validity as markers of disease progression. Among these biomarkers, ventricular enlargement is a very important measure of AD progression (Frisoni et al., 2010). Owing to the high contrast between the CSF and surrounding brain tissue on T1-weighted images, lateral ventricles can be measured more reliably than hippocampus or other structures, whose boundaries are difficult for experts to agree on (Chou et al., 2010). Furthermore, lateral ventricles span a large area within the cerebral hemispheres and abut several structures relevant to AD including the hippocampus, amygdala and posterior cingulate. Changes in ventricular morphology, such as enlargement, often reflect atrophy of the surrounding cerebral hemisphere which itself may be regionally differentiated (for example, frontotemporal in contrast to posterior cortical atrophy). Regional differences in cerebral atrophy may be reflected in specific patterns of change in ventricular morphology, so accurate analysis of ventricular morphology has the potential to both sensitively and specifically characterize a neurodegenerative process.

Many brain imaging based AD studies examine cortical and subcortical volumes (den Heijer et al., 2010; Dewey et al., 2010; Holland et al., 2009; Jack et al., 2004, 2003; Ridha et al., 2008; Vemuri et al., 2008a, 2008b; Wolz et al., 2010), but recent research (Apostolova et al., 2010a, 2010b; Chou et al., 2009a; Costafreda et al., 2011; Ferrarini et al., 2008b; Madsen et al., 2010; McEvoy et al., 2009; Morra et al., 2009; Qiu et al., 2010; Styner et al., 2005; Tang et al., 2014; Thompson et al., 2004a) has demonstrated that surface-based analyses can offer advantages over volume measures, due to their sub-voxel accuracy and the capability of detecting subtle subregional changes. Higher-order correspondences between brain surfaces are often required to be established in order to statistically compare or combine surface data obtained from different people, or at different time-points. Usually, brain surface registration is done by first mapping the surfaces to be matched onto one common canonical parameter domain, such as a sphere (Fischl et al., 1999b; Thompson et al., 2004b), or a planar rectangle (Shi et al., 2013a), and then registering the surfaces in the simpler parameter domain. The one-to-one correspondences obtained in the parameter domain induce the registration of the 3D brain surfaces. However, it is challenging to apply this framework to ventricular surfaces, due to their concave shape, complex branching topology and extreme narrowness of the inferior and occipital horns. Thus, surface-based subregional analysis of ventricular enlargement is notoriously difficult to assess, exemplified by the conflicting findings regarding genetic influences on ventricular volumes (Chou et al., 2009b; Kremen et al., 2012). Pioneering ventricular morphometry work (Paniagua et al., 2013; Styner et al., 2005) used spherical harmonics to analyze ventricular surfaces where each ventricular surface was mapped to a sphere and registered to a common template. However, as demonstrated previously (Wang et al., 2010), this spherical parameterization method may result in significant shape distortion that affects the analysis. Our prior work (Wang et al., 2007, 2011, 2010) computed the first global

conformal parameterization of lateral ventricular surfaces based on holomorphic 1-forms. However, this conformal parameterization method always introduces a singularity point (zero point, Fig. 9(a)) in the resulting parameter domain. As a result, each ventricular surface had to be partitioned into three pieces with respect to the zero point, the superior horn, the inferior horn, and the occipital horn. These three pieces were mapped to three planar rectangles and registered across subjects separately. To model a topologically complicated ventricular surface, hyperbolic conformal geometry emerges naturally as a candidate method. Hyperbolic conformal geometry has an important property that it can induce conformal parameterizations on high-genus surfaces or surfaces with negative Euler numbers and the resulting parameterizations have no singularities (Luo et al., 2008). Motivated by recent advances in hyperbolic conformal geometry based brain imaging research (Shi et al., 2013d; Tsui et al., 2013), including our own work (Shi et al., 2012; Wang et al., 2009b, 2009c), here we propose to use the hyperbolic Ricci flow method to build the canonical parameter domain for ventricular surface registration. The resulting parameterizations are angle-preserving and have no singularity points. After surface registration across subjects, surface deformations are measured by the tensor-based morphometry (TBM) (Chung et al., 2008, 2003b; Davatzikos, 1996; Thompson et al., 2000), which quantifies local surface area expansions or shrinkages. The Ricci flow method is theoretically sound and computationally efficient (Jin et al., 2008; Wang et al., 2006, 2012). In addition, TBM has been used extensively to detect regional differences in surface and volume brain morphology between groups of subjects (Chung et al., 2003b; Hua et al., 2011; Leow et al., 2009; Shi et al., 2014, 2013a, 2013b; Wang et al., 2012, 2011, 2013b). We hypothesize that the hyperbolic Ricci flow together with TBM may offer a set of accurate surface statistics for ventricular morphometry and that it may boost statistical power to detect the subtle difference between MCI patients who progress to dementia from those who fail to progress.

In this paper, we develop a ventricular morphometry system based on hyperbolic Ricci flow and TBM statistic and use it to study ventricular structural differences associated with baseline T1-weighted brain images from the ADNI dataset, including 71 patients who developed incident AD during the subsequent 36 months (MCI converter group) and 62 patients who did not during the same period (MCI stable group). These subjects were also selected based on the availability of fluorodeoxyglucose positron emission tomography (FDG-PET) data and cognitive assessment information. Here we set out to test whether our new system can detect subtle MCI conversion related changes and whether the new statistics are correlated with FDG-PET biomarkers and other cognitive measures.

Subjects and methods

Subjects

Data used in the preparation of this article were obtained from the Alzheimer's Disease Neuroimaging Initiative (ADNI) database (adni.loni.usc.edu). The ADNI was launched in 2003 by the National Institute on Aging (NIA), the National Institute of Biomedical Imaging and Bioengineering (NIBIB), the Food and Drug Administration (FDA), private pharmaceutical companies and non-profit organizations, as a $60 million, 5-year public–private partnership. The primary goal of ADNI has been to test whether serial magnetic resonance imaging (MRI), positron emission tomography (PET), other biological markers, and clinical and neuropsychological assessment can be combined to measure the progression of mild cognitive impairment (MCI) and early Alzheimer's disease (AD). Determination of sensitive and specific markers of very early AD progression is intended to aid researchers and clinicians to develop new treatments and monitor their effectiveness, as well as lessen the time and cost of clinical trials.

The Principal Investigator of this initiative is Michael W. Weiner, MD, VA Medical Center and University of California–San Francisco. ADNI is

3

the result of efforts of many coinvestigators from a broad range of academic institutions and private corporations, and subjects have been recruited from over 50 sites across the U.S. and Canada. The initial goal of ADNI was to recruit 800 subjects but ADNI has been followed by ADNI-GO and ADNI-2. To date, these three protocols have recruited over 1500 adults, ages 55 to 90, to participate in the research, consisting of cognitively normal older individuals, people with early or late MCI, and people with early AD. The follow up duration of each group is specified in the protocols for ADNI-1, ADNI-2 and ADNI-GO. Subjects originally recruited for ADNI-1 and ADNI-GO had the option to be followed in ADNI-2. For up-to-date information, see www.adni-info.org.

Based on the availability of both volumetric MRI and FDG-PET data, we selected 133 subjects from the MCI group in the ADNI baseline dataset, including 71 subjects (age: 74.77 ± 6.81) who developed incident AD during the subsequent 36 months, which we call the MCI converter group, and 62 subjects (age: 75.42 ± 7.83 years) who did not during the same period, which we call the MCI stable group. These subjects were chosen on the basis of having at least 36 months of longitudinal data. If a subject developed incident AD more than 36 months after baseline, it was assigned to the MCI stable group. All subjects underwent thorough clinical and cognitive assessment at the time of acquisition, including the Mini-Mental State Examination (MMSE) score (Folstein et al., 1975), Alzheimer's disease assessment scale—Cognitive (ADAS-COG) (Rosen et al., 1984) and Auditory Verbal Learning Test (AVLT) (Rey, 1964). The demographic information of the subjects is in Table 1.

System pipeline overview

Here we briefly overview the processing procedures in our ventricular morphometry system. Following sections are detailed explanations of each step.

Fig. 1 summarizes the overall sequence of steps in the system. First, from each MRI scan (a), we automatically segment lateral ventricular volumes with the multi-atlas fluid image alignment (MAFIA) method (Chou et al., 2010). The MR image overlaid with the segmented ventricle is shown in (b). A ventricular surface built with marching cube algorithm (Lorensen and Cline, 1987) is shown in (c). Lateral ventricle segmentation and surface reconstruction will be introduced in Section Image acquisition and preprocessing. After the topology optimization, we apply hyperbolic Ricci flow method on the ventricular surface and conformally map it to the Poincaré disk. The concepts of topology optimization and Poincaré disk model will be introduced in Section Theoretical background. Details about conformal parameterization with hyperbolic Ricci flow and embedding in Poincaré disk are in Sections Hyperbolic Ricci flow and Embedding into the Poincaré disk model, respectively. On the Poincaré disk, we compute consistent geodesics and project them back to the original ventricular surface, a method called geodesic curve lifting. The results are shown in (d). Further, we convert the Poincaré model to the Klein model where the ventricular surfaces are registered by the constrained harmonic map (Zeng et al., 2010). The registration diagram is shown in (e). Geodesic curve lifting and surface registration will be detailed in Section Geodesic curve lifting and ventricular surface constrained harmonic map via the Klein model. Next, we compute the TBM features and smooth them with the heat kernel method (Chung et al., 2005b) (f). TBM computation and its smoothing are in Section Surface tensor-based morphometry and its smoothness with heat kernel method. Finally, the smoothed TBM features are applied to analyze both group difference between the two MCI groups and correlation of ventricular shape morphometry with cognitive test scores and FDG-PET index. Significance *p*-maps are used to visualize local shape differences or correlations (g). Correction for multiple comparisons is used to estimate the overall significance (corrected *p*-values).

Image acquisition and preprocessing

High-resolution brain structural MRI scans were acquired at multiple ADNI sites using 1.5 T MRI scanners manufactured by General Electric Healthcare, Siemens Medical Solutions, and Philips Medical Systems. For each subject, the T1-weighted MRI scan was collected with a sagittal 3D MP-RAGE sequence. Typical 1.5 T acquisition parameters are repetition time (TR) of 2400 ms, minimum full excitation time (TE), inversion time (TI) of 1000 ms, flip angle of 8°, 24 cm field of view. The acquisition matrix was $192 \times 192 \times 166$ in the x, y, and z dimensions and the voxel size was $1.25 \times 1.25 \times 1.2$ mm^3. In-plane, zero-filled reconstruction (i.e., sinc interpolation) generated a 256×256 matrix for a reconstructed voxel size of $0.9375 \times 0.9375 \times 1.2$ mm^3.

The T1-weighted images from ADNI baseline dataset were automatically skull-stripped with the BrainSuite Extraction Software (Shattuck and Leahy, 2002). Then the imperfections in this automatic segmentation procedure were corrected manually. In order to adjust for global differences in brain positioning and scaling, the segmented images were normalized to the ICBM space with a 9-parameter (3 translations, 3 rotations, and 3 scales) linear transformation obtained by the Minctracc algorithm (Collins et al., 1994). After resampling into an isotropic space of 220^3 voxels with the resolution 1 mm × 1 mm × 1 mm×, the registered images were then histogram-matched to equalize image intensities across subjects. Finally, the lateral ventricular volumes were extracted using the multi-atlas fluid image alignment (MAFIA) method that combines multiple fluid registrations to boost accuracy (Chou et al., 2010). Briefly, in the MAFIA method, 6 MRI scans (2 AD, 2 MCI, and 2 normal) after preprocessing were randomly chosen from the ADNI baseline dataset. The lateral ventricles were manually traced in these 6 images following the delineation protocol described in http://resource.loni.usc.edu/resources/downloads/research-protocols/segmentation/lateral-ventricle-delineation. These labeled images are called atlases and segmentation of lateral ventricles in other unlabeled images was done by fluidly registering the atlases to all other images. For details of this method, please refer to (Chou et al., 2010).

After obtaining the binary segmentations of the lateral ventricles, we used a topology-preserving level set method (Han et al., 2003) to build surface models. Based on that, the marching cube algorithm (Lorensen and Cline, 1987) was applied to construct triangular surface meshes. Then, in order to reduce the noise from MR image scanning and to overcome the partial volume effects, surface smoothing was applied consistently to all surfaces. Our surface smoothing process consists of mesh simplification using "progressive meshes" (Hoppe, 1996) and mesh refinement by Loop subdivision surface (Loop, 1987). The similar procedures were frequently adopted in a number of our prior works (Colom et al., 2013; Luders et al., 2013; Monje et al., 2013; Shi et al., 2014, 2013a, 2013b; Wang et al., 2011, 2010) and our experience showed that the smoothed meshes are accurate approximations to the original surfaces with higher signal-to-noise ratio (SNR) (Shi et al., 2013a).

Theoretical background

This section briefly introduces the theoretical background necessary for the current work.

Table 1
Demographic information of studied MCI subjects in ADNI baseline dataset.

	Gender (M/F)	Education	Age	MMSE at baseline
MCI converter (n = 71)	45/26	15.99 ± 2.73	74.77 ± 6.81	26.83 ± 1.60
MCI stable (n = 62)	44/18	15.87 ± 2.76	75.42 ± 7.83	27.66 ± 1.57

Conformal deformation

Let S be a surface in $\mathbb{R}^3$ with a Riemannian metric $\mathbf{g}$ induced from the Euclidean metric. Let $u : S \to \mathbb{R}$ be a scalar function defined on S. It can be verified that $\widetilde{\mathbf{g}} = e^{2u}\mathbf{g}$ is also a Riemannian metric on S and angles measured by $\widetilde{\mathbf{g}}$ are equal to those measured by $\mathbf{g}$, i.e. the induced mapping is angle-preserving. Thus, $\widetilde{\mathbf{g}}$ is called a conformal deformation of $\mathbf{g}$ and u is called the conformal factor. Furthermore, when surface metrics change, the Gaussian curvature K of the surface will change accordingly and become $\widetilde{K} = e^{-2u}(-\Delta_{\mathbf{g}}u + K)$, where $\Delta_{\mathbf{g}}$ is the Laplace–Beltrami operator under the original metric $\mathbf{g}$. The

geodesic curvature k_g will become $\widetilde{k_g} = e^{-u}(\partial_{\mathbf{r}}u + k_g)$, where $\mathbf{r}$ is the tangent vector orthogonal to the boundary. The total curvature of the surface is determined by its topology with the Gauss–Bonnet theorem (Do Carmo, 1976): $\int_S K dA + \int_{\partial S} k_g ds = 2\pi\chi(S)$, where dA is the surface area element, ∂S is the boundary of S, ds is the line element, and $\chi(S)$ is the Euler characteristic number of S.

Uniformization theorem

Given a surface S with Riemannian metric $\mathbf{g}$, there exist an infinite number of metrics that are conformal to $\mathbf{g}$. The uniformization theorem
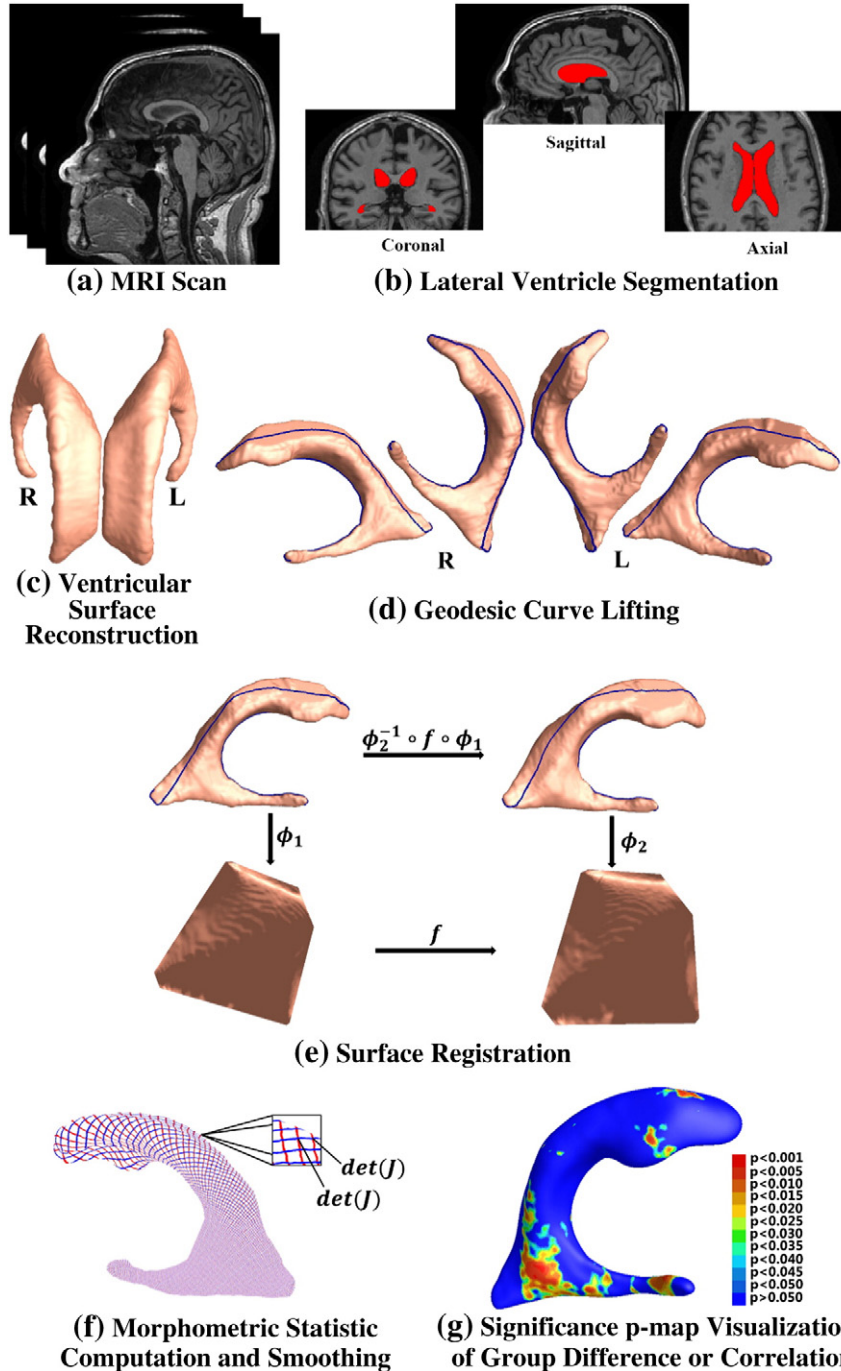

Fig. 1. A chart showing the key steps in the ventricular surface registration method. After the lateral ventricles were segmented from MRI scans and surfaces were reconstructed, we computed consistent geodesic curves on each ventricular surface to constrain the registration. Then the constrained harmonic map was used to obtain a correspondence field in the parameter domain represented by the Klein model, which also induced a surface registration in 3D. The statistic of TBM was computed on each point of the resulting matched surfaces. Finally the smoothed TBM features are applied to analyze both group difference between the two MCI groups and correlation of ventricular shape morphometry with cognitive test scores and FDG-PET index.
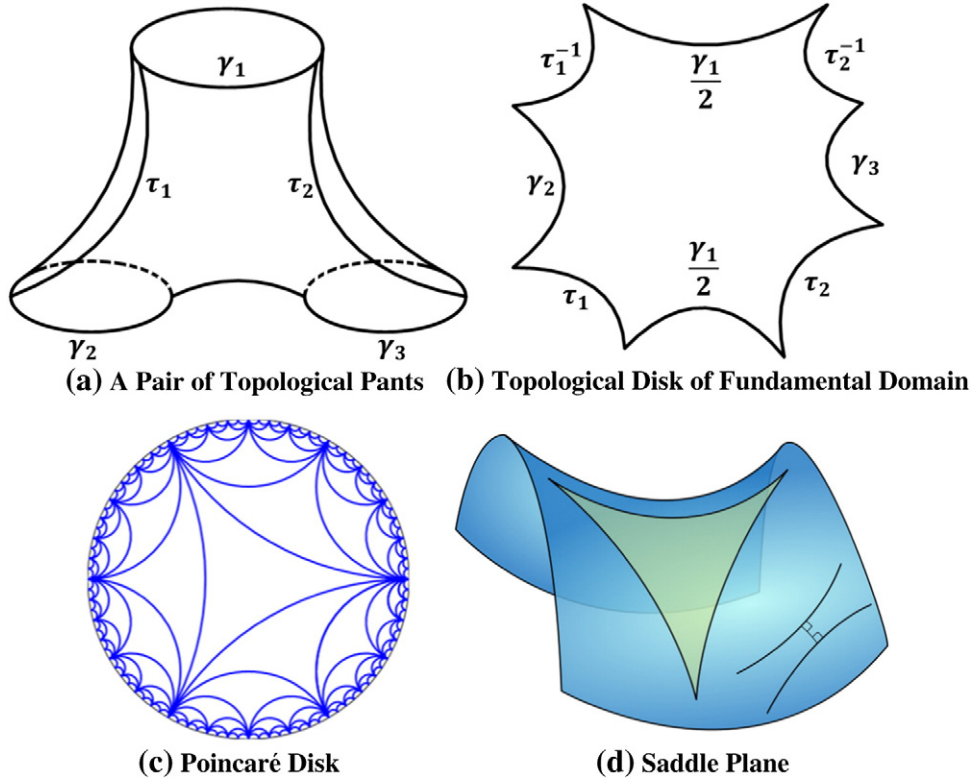
(a) A Pair of Topological Pants **(b) Topological Disk of Fundamental Domain**

(c) Poincaré Disk **(d) Saddle Plane**

Fig. 2. Illustration of hyperbolic geometry. (a) is a pair of topological pants with three boundaries γ_1, γ_2, and γ_3. τ_1 and τ_2 are automatically traced paths connecting γ_1 to γ_2, γ_1 to γ_3, respectively. After slicing along τ_1 and τ_2, the topological pants can be conformally mapped to the hyperbolic space and isometrically embedded in the topological disk of fundamental domain, as shown in (b). (c) is an illustration of the Poincaré disk model. (d) is a saddle plane which has constant negative Gaussian curvatures with a hyperbolic triangle.

states that, among all conformal metrics, there exists a unique representative which induces constant Gaussian curvature everywhere. Moreover, the constant will be one of $\{+1, 0, -1\}$. Therefore, we can embed the universal covering space of any closed surface using its uniformization metric onto one of the three canonical spaces: the unit sphere $\mathbb{S}^2$ for genus-0 surfaces with positive Euler characteristic numbers; the plane $\mathbb{E}^2$ for genus-1 surfaces with zero Euler characteristic numbers; the hyperbolic space $\mathbb{H}^2$ for high-genus surfaces with negative Euler characteristic numbers. Accordingly, we can say that surfaces with positive Euler numbers admit spherical geometry; surfaces with zero Euler numbers admit Euclidean geometry; and surfaces with negative Euler numbers admit hyperbolic geometry.

Topology optimization

Due to the concave and branching shape of the ventricular surfaces, it is difficult to find a conformal grid for the entire structure without introducing significant area distortions. Here, as in prior studies (Wang et al., 2011, 2010), we automatically located and introduced three cuts on each ventricular surface, with one cut on the superior horn, one cut on the inferior horn, and one cut on the occipital horn. The locations of the cuts are motivated by examining the topology of the lateral ventricles, in which several horns are joined together at the ventricular "atrium" or "trigone". Meanwhile, we kept the locations of the cuts consistent across subjects. This operation is called as *topology optimization* (Wang et al., 2011, 2010). After being modeled in this way, each ventricular surface becomes a genus-0 surface with 3 boundaries and is homotopic to a pair of topological pants, as shown in Fig. 2(a). Fig. 4(a) shows two different views of a ventricular surface with the three boundaries, which are denoted as γ_1, γ_2, γ_3. As a result, each ventricular surface has the Euler characteristic number -1, which means that it admits the hyperbolic geometry. In our work, we try to compute conformal mappings from ventricular surfaces to the hyperbolic space

$\mathbb{H}^2$ and use it as the canonical parameter space to register ventricular surfaces.

Poincaré disk model

As the hyperbolic space cannot be realized in $\mathbb{R}^3$, we use the Poincaré disk model to visualize it. The Poincaré disk is the unit disk $|z| < 1$, $z = x + iy$ in the complex plane with the metric $ds^2 = \frac{4dzd\bar{z}}{(1 - z\bar{z})^2}$. The rigid motion in the Poincaré disk[2] is the Möbius transformation:

$$z \rightarrow e^{i\theta}\frac{z - z_0}{1 - \overline{z_0}z} \tag{1}$$

A hyperbolic line (a geodesic) in the Poincaré disk is a circular arc which is perpendicular to the unit circle $|z| = 1$. A hyperbolic circle $circ(c, r)$ (c is the center and r is the radius) looks like a Euclidean circle $Circ(C, R)$, with $C = \frac{2 - 2\mu^2}{1 - \mu^2|c|^2}$, and $R^2 = |C|^2 - \frac{|c|^2 - \mu^2}{1 - \mu^2|c|^2}$, where $\mu = \frac{e^r - 1}{e^r + 1}$. Fig. 2(c) shows an illustration of the Poincaré disk. In order to map the ventricular surfaces to the hyperbolic Poincaré disk, we automatically traced two paths, τ_1 connecting γ_1 and γ_2 and τ_2 connecting γ_1 and γ_3, respectively, as shown in Fig. 4(b). Initially, the locations of the

---

[2] In Euclidean space, rigid motions include translation and rotation. Any transformation consisting of rigid motions changes the position of an object without deforming the shape of the object. As the Poincaré disk is a representation of the hyperbolic space, the rigid motion in it is defined by Eq. (1), which is the Möbius transformation and is different from that in the Euclidean space. However, the Möbius transformation has the same properties as the Euclidean rigid motion. For example, as shown in Fig. 4(d), the object at the center is transformed to four other different positions in the Poincaré disk with four different Möbius transformations. Each of the four pieces (shown in four colors) is a copy of the center object. They have different positions, but their shapes are the same in the hyperbolic space.

paths were not required to be consistent across subjects. But they were required to connect consistent ends of γ_1, γ_2, γ_3 for consistent surface mappings to be discussed in Section Geodesic curve lifting and ventricular surface constrained harmonic map via the Klein model. As shown in Figs. 4(a–b), endpoints with same colors were connected to each other. After slicing along the paths, a ventricular surface became a simply connected domain, which we call a topological disk. Fig. 2(b) is an illustration of the topological disk of the topological pants in Fig. 2(a), which provides the fundamental domain when embedded in the Poincaré disk.

In practice, surfaces are represented by triangular meshes. If a surface admits hyperbolic geometry, all triangles on it are hyperbolic triangles. As an illustration of the hyperbolic geometry, Fig. 2(d) shows a saddle-shape plane which has constant negative Gaussian curvatures with a hyperbolic triangle.

Hyperbolic Ricci flow

In this work we use the surface Ricci flow method (Jin et al., 2008; Wang et al., 2009c, 2006, 2012; Zeng et al., 2010) to conformally project the ventricular surfaces to the hyperbolic space and isometrically embed them in the Poincaré disk. We call this method the *hyperbolic Ricci flow method*.

Ricci flow is a powerful curvature flow method, which was first introduced in (Hamilton, 1988). Let S be a smooth surface with Riemannian metric $\mathbf{g} = (g_{ij})$, the Ricci flow deforms the metric $\mathbf{g}(t)$ according to the Gaussian curvature $K(t)$ (induced by the metric itself),

$$\frac{dg_{ij}(t)}{dt} = -2K(t)g_{ij}(t) \tag{2}$$

where t is the time parameter. Eq. (2) states that the metric should change according to the Gaussian curvature, so that the curvature evolves like a heat diffusion process. There is an analogy between the Ricci flow and heat diffusion. Suppose $T(t)$ is a temperature field on the surface, the heat diffusion equation is $\frac{dT(t)}{dt} = -\Delta_{\mathbf{g}}T(t)$, where $\Delta_{\mathbf{g}}$ is the Laplace–Beltrami operator induced by the surface metric. The temperature field becomes more and more uniform with the increase in t, and it will become constant eventually. In a physical sense, the curvature evolution induced by the Ricci flow is exactly the same as the heat diffusion on the surface as $\frac{dK(t)}{dt} = -\Delta_{\mathbf{g}(t)}K(t)$, where $\Delta_{\mathbf{g}(t)}$ is the Laplace–Beltrami operator induced by the metric $\mathbf{g}(t)$. For the proof of this analogy, please refer to (Wang et al., 2012).

With conformal mapping, which requires $\mathbf{g}(t) = e^{2u(t)}\mathbf{g}(0)$, we have a simplified Ricci flow equation

$$\frac{du(t)}{dt} = -2K(t) \tag{3}$$

the derivation of Eq. (3) can be found in Wang et al. (2012).

In engineering field, surfaces are approximated by triangular meshes. Major concepts such as metric, curvature, Ricci flow, etc., which were introduced above in the continuous setting, need to be generalized to the discrete setting. Suppose $M(V, E, F)$ is a triangular mesh, with the vertex set V, edge set E, and face set F. We define v_i the ith vertex, $[v_i, v_j]$ the edge connecting vertices v_i and v_j, and $[v_i, v_j, v_k]$ the face formed by v_i, v_j, and v_k. The discrete Riemannian metric on M is a function defined on each edge $l : E \to R^+$ such that in each face $[v_i, v_j, v_k]$, the triangle inequality holds $l_i + l_j > l_k$. Usually, it is the edge length. As shown in Fig. 3(a), the corner angles in each face are determined by the metric according to the hyperbolic cosine law:

$$\theta_i = \cos^{-1}\frac{\cosh l_j \cosh l_k - \cosh l_i}{2 \sinh l_j \sinh l_k} \tag{4}$$

Let f_{ijk} be the face formed by v_i, v_j, and v_k, and θ_i^{jk} the corner angle at v_i in this face, the discrete Gaussian curvature on v_i can be defined by the angle deficit:

$$K_i = \begin{cases} 2\pi - \sum_{f_{ijk} \in F} \theta_i^{jk} & v_i \notin \partial M \\ \pi - \sum_{f_{ijk} \in F} \theta_i^{jk} & v_i \in \partial M \end{cases} \tag{5}$$

The discrete Gaussian curvature definition is an approximation of that in the continuous setting, for the derivation, please refer to Gu and Yau (2008). Accordingly, the Gauss–Bonnet theorem also holds for the discrete meshes $\sum_{v_i \in V} K_i = 2\pi\chi(M)$ (Do Carmo, 1976).

By definition, the conformal deformation maps infinitesimal circles in one surface to infinitesimal circles in another and preserves angles among the circles. The discrete conformal deformation uses circles with finite radii to approximate the infinitesimal circles. The concept of the circle packing metric was introduced in Thurston (1976) and later adopted by Hurdal and Stephenson in their discrete cortical conformal flattening work (Hurdal and Stephenson, 2004, 2009). Fig. 3(b) shows a hyperbolic triangle together with three circles centered at its three vertices. Let Γ be a function defined on vertices $\Gamma : V \to \mathbb{R}^+$, which assigns a radius γ_i to vertex v_i. Similarly, let Φ be a function defined on edges $\Phi : E \to [0, \frac{\pi}{2}]$, which assigns an acute angle ϕ_{ij} to edge e_{ij} and is called a weight function of the edge. The pair of vertex radius function and edge weight function, (Γ, Φ), is called the *circle packing metric* of M. As shown in Stephenson (2005); Wang et al. (2012); and Zeng et al. (2010), the circles in the circle packing metric are not necessarily tangent to each other, they can intersect (Wang et al., 2012), or not intersect at all (Zeng et al., 2010). As shown in Fig. 3(b), for each triangle $[v_i, v_j, v_k]$, one can compute the Riemannian metrics by the hyperbolic cosine law:

$$l_k = \cosh^{-1}\left(\cosh \gamma_i \cosh \gamma_j + \cos \phi_{ij} \sinh \gamma_i \sinh \gamma_j\right) \tag{6}$$

Let $U : V \to \mathbb{R}$ be the discrete conformal factor and (Jin et al., 2008; Zeng et al., 2010),

$$u_i = \log\left(\tanh\frac{\gamma_i}{2}\right) \tag{7}$$

we define the discrete Ricci flow as

$$\frac{du_i}{dt} = -2K_i \tag{8}$$

The discrete Ricci flow is in the exact same form as the smooth Ricci flow (Eq. (3)). Let $U = (u_1, u_2, ..., u_n)$ be the conformal factor vector, where n is the number of vertices on M, and $U_0 = (0, 0, ..., 0)$, then the discrete hyperbolic Ricci energy is defined as (Jin et al., 2008)

$$E(U) = \int_{U_0}^{U} \sum_{i=1}^{n} K_i du_i \tag{9}$$

Given the definitions (4), (6) and (7), by direct computations, we get $\frac{\partial\theta_i}{\partial u_j} = \frac{\partial\theta_j}{\partial u_i}$. Considering the definition of K_i (Eq. (5)), immediately we get $\frac{\partial K_i}{\partial u_j} = \frac{\partial K_j}{\partial u_i}$. Thus, the differential 1-form $\omega = \sum_{i=1}^{n} K_i du_i$ is closed as $d\omega = 0$. This proves that the hyperbolic Ricci energy (Eq. (9)) is convex and its unique global minimum corresponds to the hyperbolic metric with zero vertex Gaussian curvatures. The discrete Ricci flow is the negative gradient flow of the hyperbolic Ricci energy.

The algorithm with gradient descent is summarized as following:

(1) Compute the initial radius γ_i for each vertex v_i, and weight ϕ_{ij} for each edge e_{ij} with the hyperbolic cosine law;
(2) Set the target Gaussian curvature as zero;

(a) Hyperbolic Cosine Law   **(b) Circle Packing Metric**
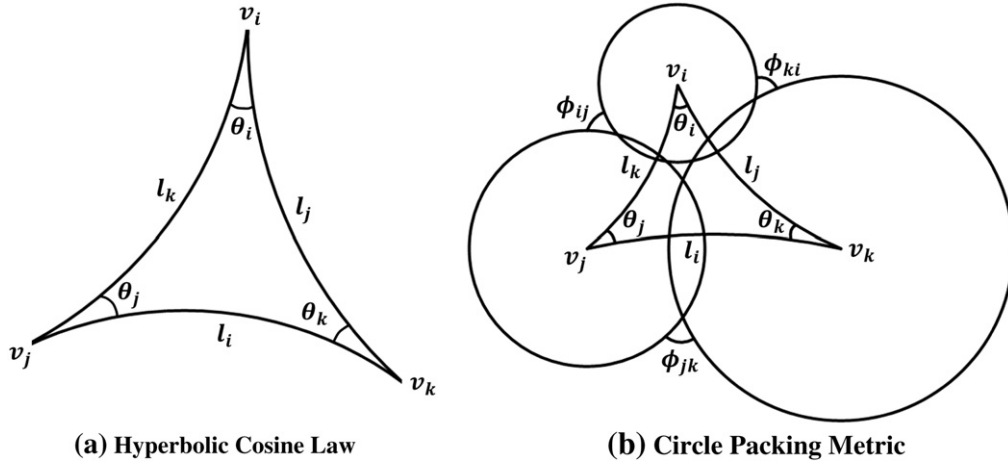
Fig. 3. Illustration of the hyperbolic cosine law (a) and visualization of the circle packing metric on a hyperbolic triangle (b).

(3) Compute edge lengths with Eq. (6), face corner angles with Eq. (4), and the Gaussian curvature with Eq. (5).

(4) Update u_i for each vertex v_i with Eq. (8) as $u_{i+1} = u_i - 2\Delta t K_i$.

(5) Update γ_i with Eq. (7).

(6) Repeat steps (3) to (5) until the final Gaussian curvature is no greater than a user-specified error tolerance.

Instead of gradient descent, the Ricci energy (Eq. (9)) can also be optimized by Newton's method (Jin et al., 2008; Wang et al., 2012), which requires compute the Hessian matrix. Let $H = (h_{ij})$ be the Hessian matrix, then

$$h_{ij} = \frac{\partial K_i}{\partial u_j}, \quad h_{ii} = \frac{\partial K_i}{\partial u_i}$$

In our experiments, we have used the Newton's method to optimize the Ricci energy, which is stable and fast. For a ventricular surface with more than 50 K vertices, the optimization took less than 30 s on a 2.66 GHz Intel Quad CPU Q8400 PC with Windows 7 64-bit operating system.

Embedding into the Poincaré disk model

After computing the discrete hyperbolic metric of a surface, we can embed this surface into the Poincaré disk. In the beginning, we select a seed face f_{012} and compute the positions of the vertices v_0, v_1, and v_2 in the Poincaré disk as following:

$$p(v_0) = (0,0), \ p(v_1) = \frac{e^{l_{01}} - 1}{e^{l_{01}} + 1}(1,0), \ p(v_2)$$
$$= \frac{e^{l_{02}} - 1}{e^{l_{02}} + 1}\left(\cos\theta_0^{12}, \ \sin\theta_0^{12}\right)$$

Then we propagate the embedding to other faces. We put all un-embedded faces adjacent to the current face into a queue. We pop a face f_{ijk} from the queue and check whether all its vertices have been embedded. If so, we continue to pop the next face from the queue. Otherwise, suppose that v_i and v_j are embedded, then $p(v_k)$ can be computed as one of the two intersections between two hyperbolic circles, $circ(p(v_i), l_{ki})$ and $circ(p(v_j), l_{kj})$, satisfying $(p(v_j) - p(v_i)) \times (p(v_k) - p(v_i)) > 0$. We continue to do so until the queue is empty. Fig. 4(c) shows the embedding of the ventricular surface in the Poincaré disk. The boundaries γ_1, γ_2, and γ_3 have become geodesics $\frac{\gamma_1}{2}, \frac{\gamma_1}{2}, \gamma_2,$ and γ_3. We call it as the *Poincaré disk embedding* of the fundamental domain of the surface. As pointed out in Jin et al. (2008), different selections of the seed face will result in different layouts of the fundamental domain. In this work, to keep the fundamental domain consistency across

subjects, we first applied our prior holomorphic 1-form method (Wang et al., 2011, 2009e) to compute a Euclidean conformal mapping and automatically chose the seed face at the center of the zero point region (Wang et al., 2007), as shown in Fig. 9(a).

The computed boundaries of the fundamental domains of different ventricular surfaces are not consistent, i.e., the positions of τ_1 and τ_2 may not be consistent. We further apply a geodesic lifting step to achieve consistent boundaries with the deck transformation group generators. For a surface with hyperbolic geometry, its universal covering space is the entire Poincaré disk. As shown in Fig. 4(c), there are 4 free sides in the fundamental domain, τ_1 and τ_2 and their compliments τ_1^{-1} and τ_2^{-1} (after we cut along a curve, it generates two boundaries on the new surface, one is τ_1 and its compliment is τ_1^{-1}). The rigid transformations across these sides induce different periods of the surface mapping. In Poincaré disk, all rigid motions are Möbius transformations. There exist unique Möbius transformations map τ_1 to τ_1^{-1} and τ_2 to τ_2^{-1}, respectively, as shown in Fig. 4(d). We explain the details for computing the Möbius transformation that maps τ_1 to τ_1^{-1}. Counterclockwisely, let the starting and ending vertices of the two sides be $\partial\tau_1 = (p_0, q_0)$ and $\partial\tau_1^{-1} = (q_1, p_1)$. The geodesic distance from p_0 to q_0 equals the geodesic distance from p_1 to q_1 in the Poincaré disk. To align them, we first compute a Möbius transformation t_0, which maps p_0 to the origin and q_0 to a positive real number, with

$$t_0 = e^{i\theta_0} \frac{z - p_0}{1 - \overline{p_0}z}, \quad \theta_0 = arg\frac{p_0 - q_0}{1 - \overline{p_0}q_0}$$

Similarly, we can compute another Möbius transformations t_1, which maps p_1 to the origin and q_1 to a positive real number. Then with $t_0(q_0) = t_1(q_1)$, we get the final Möbius transformation $t = t_1^{-1} \circ t_0$, which satisfies $p_1 = t(p_0)$ and $q_1 = t(q_0)$. Any deck transformation can be composed by the generators. Then the universal covering space can be tiled by transforming a fundamental domain by the deck transformations and gluing the transformed fundamental domains with the original fundamental domain. Fig. 4(d) shows a portion of the universal covering space, which is tiled by 5 fundamental domains, one original and 4 transformed by the 4 deck transformation group generators.

Geodesic curve lifting and ventricular surface constrained harmonic map via the Klein model

To register brain surfaces, a common approach is to compute a range of intermediate mappings to a canonical parameter space, such as a sphere (Bakircioglu et al., 1999; Fischl et al., 1999b; Gu et al., 2004; Yeo et al., 2010) or a planar domain (Auzias et al., 2013; Joshi et al., 2007; Thompson et al., 2004b; Thompson and Toga, 2002; Wang et al.,
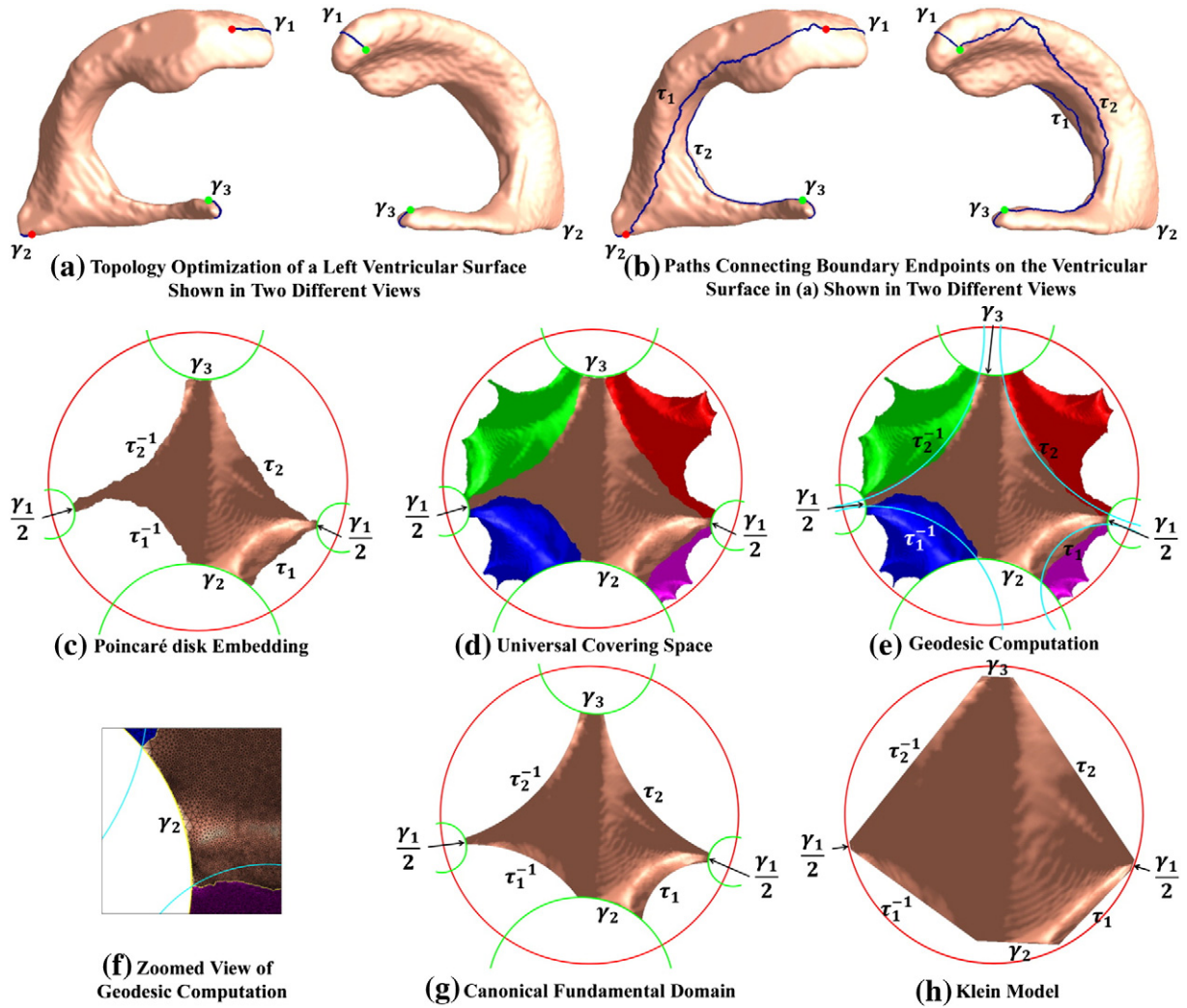
(a) Topology Optimization of a Left Ventricular Surface Shown in Two Different Views

(b) Paths Connecting Boundary Endpoints on the Ventricular Surface in (a) Shown in Two Different Views

(c) Poincaré disk Embedding

(d) Universal Covering Space

(e) Geodesic Computation

(f) Zoomed View of Geodesic Computation

(g) Canonical Fundamental Domain

(h) Klein Model

Fig. 4. A chart showing the computation of geodesic curves for a ventricular surface. After introducing one cut on each horn by topology optimization, the ventricular surface became a genus-0 surface with 3 boundaries, which is homotopic to a pair of topological pants (a). We traced two paths connecting consistent endpoints of the boundaries, i.e., the endpoint pair with the same color (b). We then computed the hyperbolic metric of the ventricular surface with hyperbolic Ricci flow and isometrically embedded it onto the Poincaré disk. (c) is the topological disk fundamental domain, which was obtained by slicing (b) along the paths and embedding it on the Poincaré disk with the hyperbolic metric. (d) is a portion of the universal covering space of the ventricular surface, tiled by 5 fundamental domains, which were obtained with the deck transformation group generators. In (d), we computed geodesic curves, i.e., hyperbolic circle arcs (e). The geodesic curves were consistent across subjects as we constrained them to connect consistent endpoints of existing geodesics γ_1, γ_2, and γ_3. (f) shows a zoomed view of the geodesic curves. After slicing the universal covering space along the geodesic curves, we got a consistent fundamental domain for each ventricular surface, which we call the canonical fundamental domain (g). Finally, we converted (g) to the Klein model (h), which is a Euclidean polygon. The Klein model was used as the canonical parameter space for ventricular surface registration.

2013b, 2010). In the current work, we propose to use the Klein model as the canonical space to register ventricular surfaces.

First, we use the Poincaré disk model to achieve consistent geodesic curves across ventricular surfaces. As shown in Fig. 4(c), $\frac{\gamma_1}{2}$, $\frac{\gamma_1}{2}$, γ_2, and γ_3 are already geodesics on the Poincaré disk model, but the paths between them, τ_1, τ_2, τ_1^{-1}, and τ_2^{-1}, are not. Fig. 4(b) shows the paths on the original surface. If the positions of the paths are not consistent across subjects, the fundamental domains will also be different for different surfaces. We solve this problem by locating the geodesic on the Poincaré disk between two fixed points and mapping it back to the original surface, a step known as *geodesic curve lifting*. Specifically, each of these geodesics is an arc on a circle which passes two fixed points in the Poincaré disk and is orthogonal to the unit circle. Thus the geodesics are unique. The fixed points are the endpoints of existing geodesics. For example, as shown in Fig. 4(e), τ_1 is an arc on the circle which passes one endpoint of $\frac{\gamma_1}{2}$ and one endpoint of γ_2 and is orthogonal to $|z| = 1$. As we stated in Section Theoretical background, the initial paths τ_1 and τ_2 can be inconsistent, but they have to connect consistent endpoints of γ_1, γ_2, and γ_3, as to guarantee the consistency of the geodesic

curve computation. After slicing the universal covering space along the geodesics, we get the canonical fundamental domain, as shown in Fig. 4(g). All the boundary curves become geodesics. As the geodesics are unique, they are also consistent when we map them back to the surface in $\mathbb{R}^3$. As shown in Fig. 5, the first row shows a left ventricular surface from the MCI stable group and second row shows one from the MCI converter group. We can see that, although the two surfaces have different shapes due to disease progression, the geodesics τ_1 and τ_2 on them are consistent.

Furthermore, we convert the Poincaré model to the Klein model with the following transformation (Zeng et al., 2010),

$$z \rightarrow \frac{2z}{1 + \overline{z}z} \tag{10}$$

It converts the canonical fundamental domains of the ventricular surfaces to a Euclidean octagon, as shown in Fig. 4(h). Then we use the Klein disk as the canonical parameter space for the ventricular surface registration.
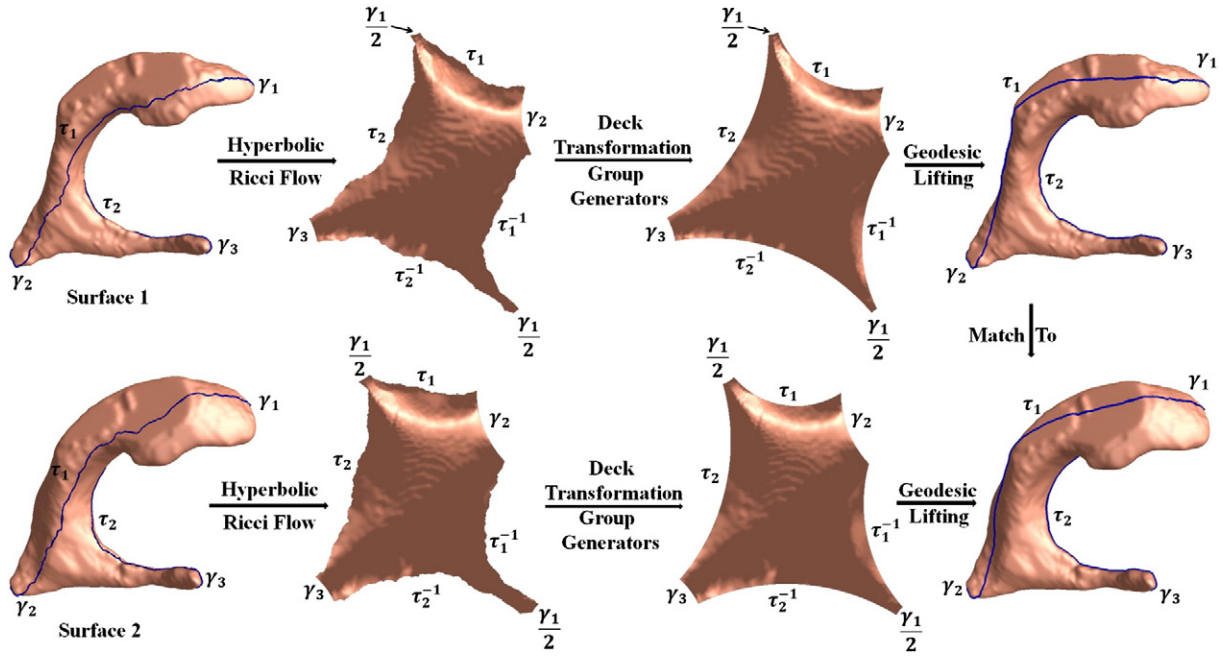
Fig. 5. Illustration of ventricular surface registration with the hyperbolic Ricci flow and geodesic curve lifting. Surface 1 and surface 2 were from the MCI stable group and MCI converter group, respectively. After computing their canonical fundamental domains with the steps in Fig. 4, we lifted the computed geodesic curves to the original surfaces. The last column shows that the geodesic curves introduced by our method are consistent across subjects. Then the surfaces were registered by constrained harmonic map with consistent geodesic curve matching.

In our experiment, 133 left and 133 right ventricular surfaces were registered to a common left and right template, respectively. The templates are the left and right ventricular surfaces from a randomly selected subject. We implemented the octagon constrained harmonic map (Wang et al., 2012, 2011). Briefly, the constrained harmonic map was computed by solving the Laplace equation with the Dirichlet boundary condition. Suppose M, N are two ventricular surfaces with their Klein disks, the map $f : M \rightarrow N$ is a harmonic map if $\Delta f = 0$. In order to solve the Laplace equation, all the boundary curves in the Klein octagon disk were treated as boundary conditions and enforced to be aligned across subjects with linear interpolation by the arc length parameter. To show the correspondences between boundaries, we assigned unique labels to geodesic boundaries shown in Fig. 5.

Surface tensor-based morphometry and its smoothness with heat kernel method

In this work we use surface tensor-based morphometry (TBM) (Chung et al., 2008; Davatzikos, 1996; Thompson et al., 2000) to analyze the ventricular shape changes along with disease progression. Suppose $\phi : S_1 \rightarrow S_2$ is a map from surface S_1 to surface S_2. The derivative map of ϕ is the linear map between the tangent spaces $d\phi : TM(p) \rightarrow TM(\phi(p))$, induced by the map ϕ, which also defines the Jacobian matrix of ϕ. In the triangle mesh surface, the derivative map $d\phi$ is approximated by the linear map from one face $[v_1, v_2, v_3]$ to another $[w_1, w_2, w_3]$. First, the surfaces $[v_1, v_2, v_3]$ and $[w_1, w_2, w_3]$ are isometrically embedded onto the Klein disk, the planar coordinates of the vertices v_i and w_i are denoted by the same symbol v_i and w_i. Then the Jacobian matrix for the derivative map $d\phi$ can be explicitly computed as (Wang et al., 2009a)

$$J = d\phi = [w_3 - w_1, w_2 - w_1][v_3 - v_1, v_2 - v_1]^{-1} \tag{11}$$

Then the TBM is defined as $\sqrt{\det(J)}$. TBM measures the amount of local area changes in a surface with the map ϕ (Chung et al., 2008).

As pointed out in (Chung et al., 2005b, 2003a), in an integrated surface analysis system, each step in the processing pipeline including MR image acquisition, image segmentation, surface reconstruction,
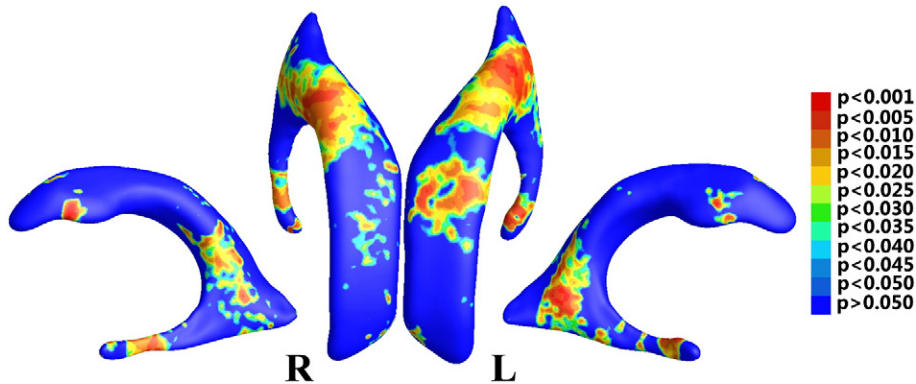

Fig. 6. Illustration of statistical map showing local shape differences (*p*-values) between MCI converter and MCI stable groups from the ADNI baseline dataset, based on tensor-based morphometry (TBM), which was smoothed by the heat kernel smoothing method (Chung et al., 2005b).

etc., are expected to introduce noise in the deformation measurement. To account for the noise effects, we apply the heat kernel smoothing algorithm proposed in (Chung et al., 2005b) to increase the SNR in the TBM statistical features and boost the sensitivity of statistical analysis. We briefly describe the smoothing method as follows, for details please refer to (Chung et al., 2005b).

Let S be a surface and $p \in S$ be a point on S. Y is a real-valued function defined on S, representing a measurement of the surface, e.g., the TBM features in our study. Consider a stochastic model for Y as $Y(p) = \theta(p) + \epsilon(p)$, where θ is the unknown mean measurement and ϵ is a zero mean Gaussian random field. The heat kernel smoothing estimator of θ is defined by the convolution

$$\bar{\theta}(p) = K_\sigma * Y(p) = \int_S K_\sigma(p,q) Y(q) d\mu(q) \tag{12}$$

where q is a point on S which is adjacent to p, $\mu(q)$ is the surface Lebesgue measure, and σ is the smoothing parameter (bandwidth). In numerical implementation, if σ is sufficiently small and q is sufficiently close to p, the heat kernel is defined as:

$$K_\sigma(p,q) \approx \frac{1}{\sqrt{2\pi\sigma}} \exp\left[-\frac{d^2(p,q)}{2\sigma^2}\right] \tag{13}$$

where $d(p,q)$ is the geodesic distance between p and q. Heat kernel smoothing with large bandwidth can be decomposed into iterated kernel smoothing with small bandwidth via

$$K_\sigma^{(m)} * Y = \underbrace{K_\sigma * K_\sigma * \dots * K_\sigma * Y}_{m \text{ times}} = K_{\sqrt{m}\sigma} * Y \tag{14}$$

For the case at hand, we define $N_p = \{q_0, q_1, \dots, q_k\}$ to be the set of neighboring points of p on S and the normalized truncated kernel for S to be

$$W_\sigma(p, q_i) = \frac{\exp\left[-\dfrac{d^2(p,q_i)}{2\sigma^2}\right]}{\sum_{j=0}^{k} \exp\left[-\dfrac{d^2(p,q_j)}{2\sigma^2}\right]} \tag{15}$$

The discrete convolution is defined as $W_\sigma * Y(p) = \sum_{i=0}^{k} W_\sigma(p, q_i) Y(q_i)$.

Ventricular surface morphometry analysis of MCI group differences study

To evaluate whether ventricular morphometry, analyzed in this way, could be a valid predictive biomarker, we studied morphological differences in the lateral ventricles extracted from the baseline MR images between the two different MCI groups. We applied Student's t test on the TBM statistic to study group difference; we used permutation tests to correct for multiple comparisons (Nichols and Holmes, 2002). Given two groups of ventricular surfaces, on each surface point, we compute a t value with true group labels to represent the difference between the two groups of subjects on this point. We then randomly assign the ventricular surfaces into two groups with same number of subjects in each group as in the true grouping and re-compute the t value on each surface point, which we denote as the t' value. The random group assignment is permuted 5000 times and results in 5000 t' values on each point. A probability on each surface point is computed as the ratio of the number of t' values which are greater than the t value to the number of total permutations. These probability values (p-values) are color coded on an average ventricular shape to build the significance p-map (uncorrected) of the group comparison. Given a pre-defined statistical threshold of $p = 0.05$, the feature in a

significance p-map is defined as number of surface points with p-values lower than this threshold, which is also regarded as the real effect in the true experiment. The feature is then compared with features that occur by accident in the random groupings. A ratio is computed describing the fraction of the time an effect of similar or greater magnitude to the real effect occurs in the random assignments. This ratio is the chance of the observed pattern occurring by accident and provides an *overall significance value of the map* (corrected for multiple comparisons) (Thompson et al., 2003).

Correlation between ventricular shape and cognition and other AD biomarkers

In addition to examining the group difference, we also investigated the ventricular shape morphometry correlation with each of several cognitive tests such as the 11-item Alzheimer's Disease Assessment Scale-Cognitive (ADAS-COG11) (Rosen et al., 1984), and with the FDG-PET based hypometabolic convergence index (HCI) (Chen et al., 2011), which is computed from the same subject's FDG-PET image and is a single measurement of the extent to which the pattern and magnitude of cerebral hypometabolism in an individual's FDG-PET image correspond to that in AD patients. Such correlation analysis may help evaluate whether the proposed ventricular morphometry is linked to cognition or abnormal levels of AD-related markers that were previously reported. We apply a Pearson correlation method to analyze the relationship between the ventricular shape morphometry and cognitive or FDG-PET measures, where the latter is used as the predictor. We estimate the p-value of the correlation at every surface point to build the correlation p-map. The estimated r-value, i.e., the correlation coefficient on each surface point, is also computed. Similar to group difference analysis, the overall significance value of the correlation, corrected for multiple comparisons, is obtained through a permutation test (5000 iterations) of cognitive or other AD biomarker values.

Results

Volume and area differences between diagnostic groups

We first tested if there were significant differences between two groups (MCI converter vs. stable) with two global measurements of shape changes: the total volumes and surface areas of the ventricles. In each experiment, we combined the volumes or areas of the left and right ventricles to form a 1×2 vector (V_l, V_r) or (A_l, A_r) for the permutation test with 5,000 random assignments of subjects to groups, given 0.05 as the significant level. However, neither of them detected significant differences between the groups. The permutation test corrected p-values are 0.0803 for the volume and 0.2922 for the area.

Group difference analysis with tensor-based morphometry

We performed a group comparison with Student's t test on the smoothed TBM features after we registered ventricular surfaces with our proposed method. Specifically, for all points on the ventricular surface, we ran a permutation test with 5,000 random assignments of subjects to groups to estimate the statistical significance of the areas with group differences in surface morphometry. The probability was color coded on each surface point as the statistical p-map of group difference. Fig. 6 shows the p-map of group difference detected between the MCI converter ($n = 71$) and stable ($n = 62$) groups, using the smoothed TBM as a measure of local surface area change and the significance level at each surface point as 0.05. In Fig. 6, the non-blue color areas denote the statistically significant difference areas between two groups. The overall significance of the map is 0.0172.

Correlation analysis of ventricular morphometry with cognitive measurements

We studied the correlation between the smoothed surface TBM statistic and three cognitive measurements, including MMSE score (Folstein et al., 1975), ADAS-COG11 (Rosen et al., 1984) and AVLT (Rey, 1964) on the 133 subjects with MCI. After the permutation tests, the correlation with ADAS-COG11 passed the multiple comparisons (the overall significance of the correlation value $p = 0.0110$) while the correlations with MMSE and AVLT did not pass the multiple comparisons test (the overall significance of the correlation value $p = 0.8516$ for MMSE and $p = 0.4358$ for AVLT). Fig. 7(a) shows the p-map of correlation results with ADAS-COG11, where the non-blue color areas denote the statistically significant difference areas; (b) shows the r-map of the r-values where the red color denotes a positive correlation and the blue color a negative correlation. In the statistically significant areas in Fig. 7(a), the maximum r-value is 0.3701, the average r-value is 0.1548, and the dominant correlations are positive (86.18%).

Correlation analysis of ventricular morphometry with HCI

Since all subjects included in this study had both structural MRI and FDG-PET images, we attempted to study whether ventricular morphometry features were correlated with FDG-PET based single global index HCI. If such a correlation holds, we may use MRI measures as surrogates of disease progression in AD, even in pre-clinical stages (for related work, please see (Chou et al., 2009a, 2010; Henneman et al., 2009; Vemuri et al., 2010; Whitwell et al., 2008)). In previous studies, we showed that HCI correlated with AD progression and smaller hippocampal volumes (Chen et al., 2012; Reiman and Jagust, 2012; Schraml et al., 2013; Toledo et al., 2013).

The smoothed TBM statistic of the 133 MCI patients was correlated with their HCI measurements, with the permutation test corrected p-value as 0.0001. Fig. 8(a) shows the correlation p-map color-coded with uncorrected p-values and (b) shows the r-map color-coded with the correlation coefficients. On the statistically significant areas in Fig. 8(a), the maximum r-value is 0.5163, the average r-value is 0.3030, and the dominant correlations are positive (99.40%). It is interesting to note that the enlargement of lateral ventricles in these patients was correlated with higher HCI, implicating enlarged ventricles were associated with greater glucose uptake reduction. Such positive correlation was observed in multiple locations. Of special interest and relevant to reported AD hypometabolism were the regions in the neighborhood of posterior cingulate.

Discussion

Our study has two main findings. First, we demonstrate the feasibility to apply hyperbolic geometry to register ventricular surfaces across subjects. In brain imaging, a surface-based morphometry analysis approach is to set up parametric grids on surfaces, and then use differential geometry to come up with useful descriptors of surface features of interest, or to summarize the geometry as a whole. Prior research has used sphere (Jeong et al., 2013; Lee et al., 2013; Styner et al., 2005) or Euclidean plane (Wang et al., 2011, 2010) as the parameter domain. However, for ventricular surfaces with a branching structure, as demonstrated in our prior work (Wang et al., 2010), spherical mapping creates distortions and planar mapping some inevitable singularities. The hyperbolic Ricci flow method (Wang et al., 2009b, 2009c; Zeng et al., 2010) is capable of parameterizing complex shapes. Thus it has the potential to detect subtle differences between people with high accuracy and categorize them into diseased and healthy control groups, or as in the current study categorize them into different risk levels of disease,
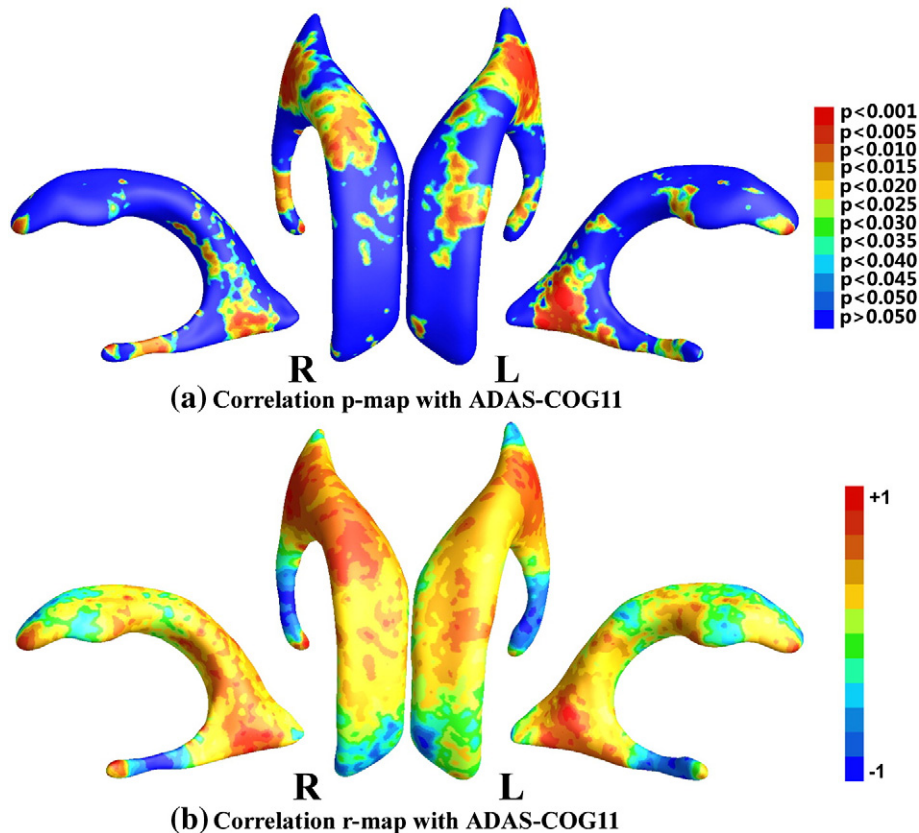

Fig. 7. Correlation maps with ADAS-COG11. (a) shows the *p*-map of correlation results with ADAS-COG11, where the non-blue color areas denote the statistically significant difference areas; (b) shows the *r*-map of the *r*-values where the red color denotes a positive correlation and the blue color a negative correlation.
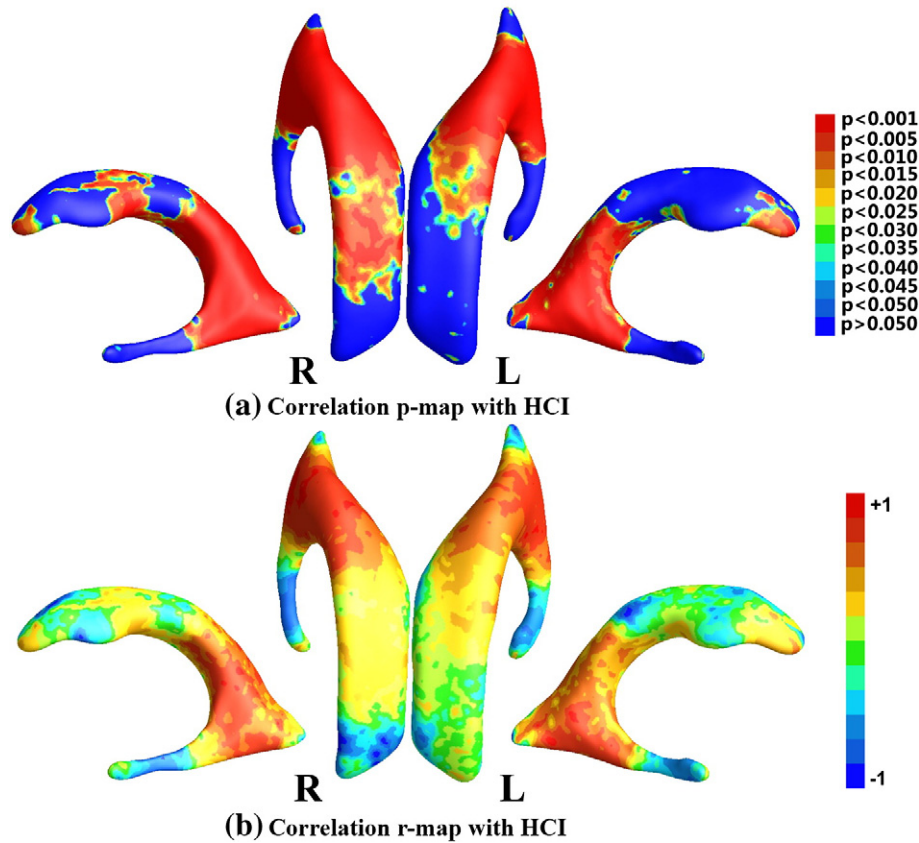
Fig. 8. Correlation maps with HCI. (a) shows the *p*-map of correlation results with HCI, where the non-blue color areas denote the statistically significant difference areas; (b) shows the *r*-map of the *r*-values where the red color denotes a positive correlation and the blue color a negative correlation.

by analyzing ventricular surface deformation tensors computed from a set of parametric surfaces using concepts from hyperbolic conformal parameterizations. In addition, the introduced hyperbolic Ricci flow method is theoretically sound and numerically efficient (Jin et al., 2008; Wang et al., 2012; Zeng et al., 2010). Together with geodesic curve lifting and the Klein model, our proposed computational framework may achieve a diffeomorphic ventricular surface registration with consistent boundary matching condition. Second, the surface tensor-based morphometry, which is computable from the conformal grid, carries rich information on local surface geometry that is defined at the coordinates of the well-organized surface grid. As demonstrated in many prior studies (Chung et al., 2008, 2003b; Davatzikos, 1996; Thompson et al., 2000), the resulting set of surface tensor methods practically encodes a great deal of information that would otherwise be inaccessible, or overlooked. The analysis of parametric meshes for computational studies of ventricular structures can be made more powerful by analyzing the surface metric tensor information inherent in the surface.

We validated our proposed methods in our ongoing work on MCI conversion prediction (Chen et al., 2013) which examined baseline measurements of structural MRI and FDG-PET, in combination with cognitive tests, to distinguish individuals with MCI who developed incident AD from those who did not, with the aim of establishing their usefulness as predictors for progression to AD. Our current work focused on ventricular morphometry analysis. Although the analyses of global ventricular volume and surface area did not differentiate

MCI converter and MCI stable groups, our fine-grained analysis revealed significant differences mostly localized around the subregion of the ventricular body that abuts medial temporal lobe structures. This subregional ventricular enlargement was reported to correlate with atrophy of medial temporal lobe which includes the hippocampal

formation. Consistent with prior observations, e.g. (Frisoni et al., 2010; Thompson et al., 2003), our findings suggest that grey matter atrophy starts from the temporal lobe region and then spreads to involve frontal cortices, consistent with Braak staging of neurofibrillary pathology (Braak et al., 2006). Importantly, they provide evidence that ventricular subfield analysis provides enhanced statistical power in structural MRI analysis compared with ventricular volume analysis. Some recent studies (Li et al., 2012; Weiner et al., 2012; Westman et al., 2013) found that including optimum features from multiple modalities provides better AD predictive value than any one measure alone. The proposed ventricular surface TBM features may enhance the predictive value of MRI-derived data in AD research.

Furthermore, the positive correlation between ventricular morphometry and ADAS-COG11 that we found is consistent with previous studies that correlated ventricular expansion with worsening cognition in MCI subjects (Jack et al., 2009; Samtani et al., 2012). The strong positive correlation with HCI values supports to the validity of our algorithm and demonstrates the linkage between functional abnormalities and structural changes (ventricle enlargement particularly in our study). As shown in the Results section, we found that the ventricular subregions where the statistically significant correlation between ventricle enlargement and HCI abutted areas of earliest FDG-PET change in AD, particularly the posterior cingulate (Buckner et al., 2008; Leech and Sharp, 2014; Matsuda, 2007a), and to our knowledge, this is the first study to explore the relationship between ventricular measures and FDG-PET measures.

Applicability to other brain structures

As stated by the uniformization theorem, any surface with a negative Euler characteristic number admits a hyperbolic background geometry

and can be conformally mapped to the hyperbolic space $\mathbb{H}^2$. Geometrically, the Euler characteristic number is defined as $2 - 2g$ for closed surfaces, where g is the surface genus, i.e., the number of handles on a surface, and is defined as $2 - 2g - b$ for surfaces with boundaries, where b is the number of boundaries. Thus the hyperbolic Ricci flow method has broad applicability in human brain surface morphometry studies, as surfaces of brain structures are often irregular and topologically complicated. Here we take the cortical surface as an example. In human brain mapping field, a diffeomorphic mapping between a pair of cortical surfaces with landmark correspondence is usually pursued to study brain deformations along with disease progression. By slicing a cortical surface open along three or more landmark curves, the cortical surface becomes a genus-0 surface with multiple boundaries, which has a negative Euler number. In our prior work (Shi et al., 2012), we illustrated the application of our method on a cortical surface with three landmark curves, which is

homotopic to the topological pants. For cortical surfaces with more landmarks, which also have negative Euler numbers, the hyperbolic Ricci flow method is still applicable (Shi et al., 2013c, 2013d), so the remaining processes of the proposed method follow naturally. On the other hand, for different brain structures, certain processing steps in the pipeline may need to be adapted accordingly. For example, a major difference between cortical and ventricular surface processing with the proposed method is the topology optimization. Given the highly variable gyral patterns of cortical surfaces, one may need to work with experienced neuroanatomists to manually label homologous landmark curves across subjects following some well-established anatomical protocols such as (Sowell et al., 2002), as described in our prior work (Wang et al., 2012, 2013b). In this case, the topology optimization reduces to slicing a cortical surface along a set of manually defined landmark curves to change it into a genus-0 surface with multiple boundaries.
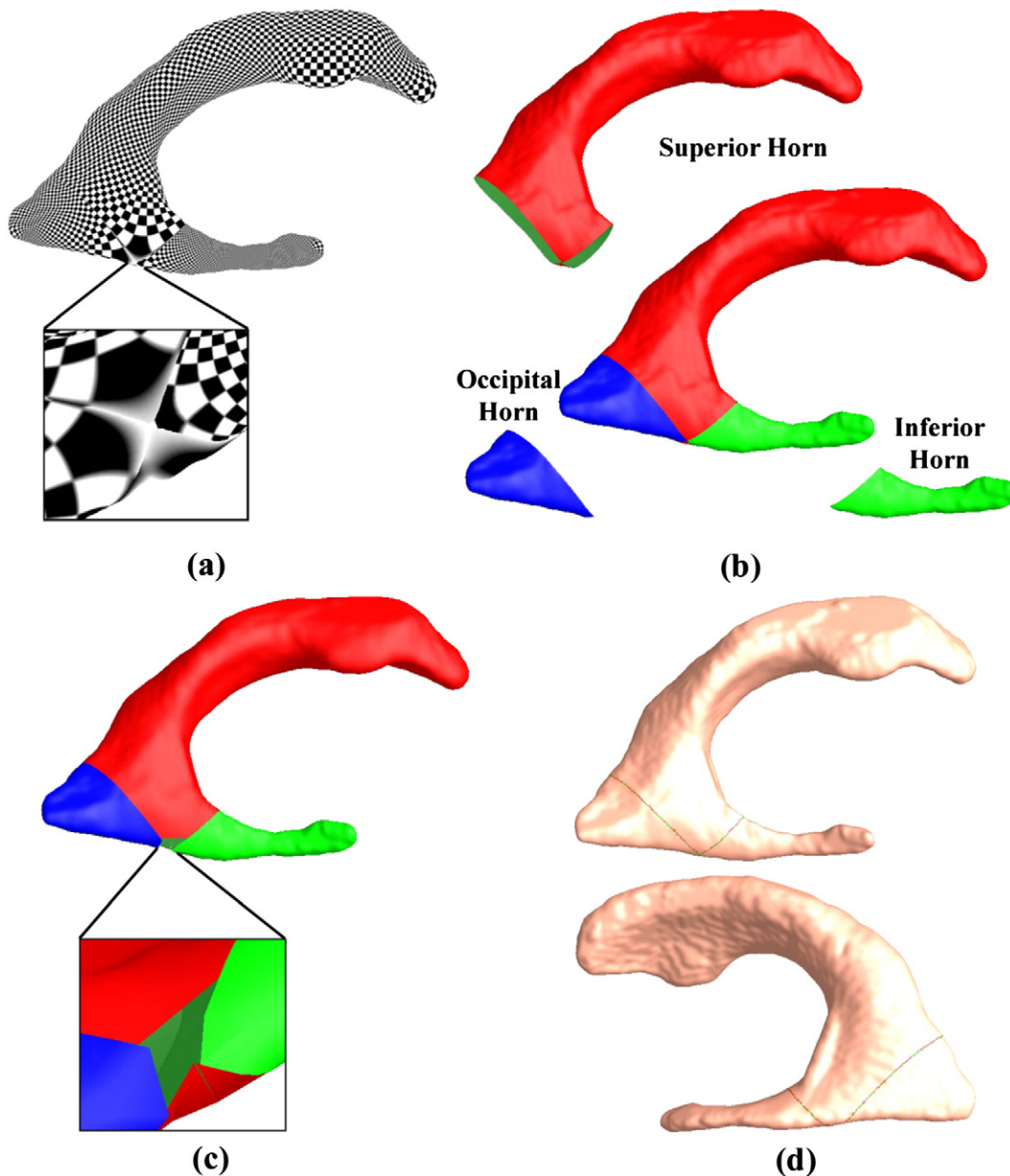

Fig. 9. Lateral ventricular surface parameterization with a method based on holomorphic 1-forms (Wang et al., 2009d). Due to the property of holomorphic 1-forms, the ventricular surface parameterization has a zero point (a). In (Wang et al., 2009d), the ventricular surface was segmented with curves traced from the zero point and each horn was mapped to the parameter domain and registered separately (b). After registering each part separately and merging them back together, the ventricular surface has a hole at the zero point position (c). Surface registration is also affected by the locations of the cuts that divide a ventricular surface into three parts (d).

Comparison with holomorphic 1-form algorithm

The holomorphic 1-form algorithm (Wang et al., 2009d) is a commonly used method to analyze lateral ventricular surfaces (Wang et al., 2011). However, due to the limitation of holomorphic 1-form itself, this method introduces singularities and the number of singularities equals the absolute value of the Euler characteristic number of a surface. In analyzing lateral ventricular surfaces, each surface has a singular point, as shown in Fig. 9(a), which was called zero point in Wang et al. (2009d) and Wang et al. (2011) and used as the starting point to segment a ventricular surface into three parts, the superior horn, the inferior horn, and the occipital horn, as shown in Fig. 9(b). After registering the three horns separately and merging them to form the whole registered ventricular surface, a hole is generated around the zero point due to the changes from surface registration, as shown in Fig. 9(c), which is not reasonable in analyzing anatomical surfaces. On the other hand, the new registration introduces no holes as shown in Fig. 6. Furthermore, the segmentation of ventricular surfaces with holomorphic 1-form, though consistent, separates an entire surface into independent partitions. The independent registrations of different partitions are based on matching surface features which should not be separated. For example, when registering the superior horn, the other two horns are not affected, which may not be true when registering the ventricular surfaces as a whole. Particularly, as shown in Fig. 6, as most of the significantly different areas concentrated at the locations of the partition cuts, the statistical analysis may be affected by the segmentations. Another problem with the ventricular surface segmentation is that the surface registration may be affected by the locations of the cuts that divide a ventricular surface into three parts. As shown in Fig. 9(d), we slightly changed the locations of the cuts on a left ventricular surface (shown in two different views), where the original cuts are shown in green, and the changed cuts are shown in red. Although the cutting locations almost overlap, the resulting registered ventricular surfaces are different. By measuring the differences with the Euclidean distances between pairs of vertices on the two registered surfaces, the differences are in the range of [0.0001, 1.3545]. Even more careful studies are necessary to determine the impact of the cutting locations on the statistical analysis. Thus it is advantageous for the new algorithm as it takes the ventricular surface as an entirety for the registration.

Comparison with SPHARM

SPHARM (Styner et al., 2006) is another surface mapping tool with a number of applications (Alhadidi et al., 2012; Paniagua et al., 2012, 2013; Tae et al., 2011). It takes a binary image segmentation as input and provides functions such as surface reconstruction, spherical harmonic mapping and surface registration; statistical analysis tools are also included. The major limitation of SPHARM is that it assumes the input binary image segmentation has a spherical topology. Thus prior work on ventricular shape morphometry with SPHARM usually discarded the inferior horn (Gerig et al., 2001; Paniagua et al., 2013). The inclusion of the long and narrow inferior horn in our segmentation makes the shape of the lateral ventricle non-spherical. As a result, SPHARM cannot successfully parameterize the concave ventricular surfaces that are reconstructed from our segmentation unless a coarse resolution is used. For this experiment, we resampled the segmented binary images into a resolution of $2 \times 2 \times 2$ mm^3. However, the resulting spherical parameterizations still have severe distortion and overlap on the inferior horn, as shown in Fig. 10(a), and 22 subjects failed the parameterization process. After surface registration, the TBM statistic was computed at each vertex of the aligned surfaces as described in Section Surface tensor-based morphometry and its smoothness with heat kernel method and group difference was analyzed as in Section Ventricular surface morphometry analysis of MCI group differences study. The significance *p*-map of group comparison between 58 converters and 53 stable MCI subjects with SPHARM is shown in Fig. 10(b). The result of our method is shown in Fig. 10(c) and the cumulative distribution function (CDF) plots in Fig. 10(d) show the
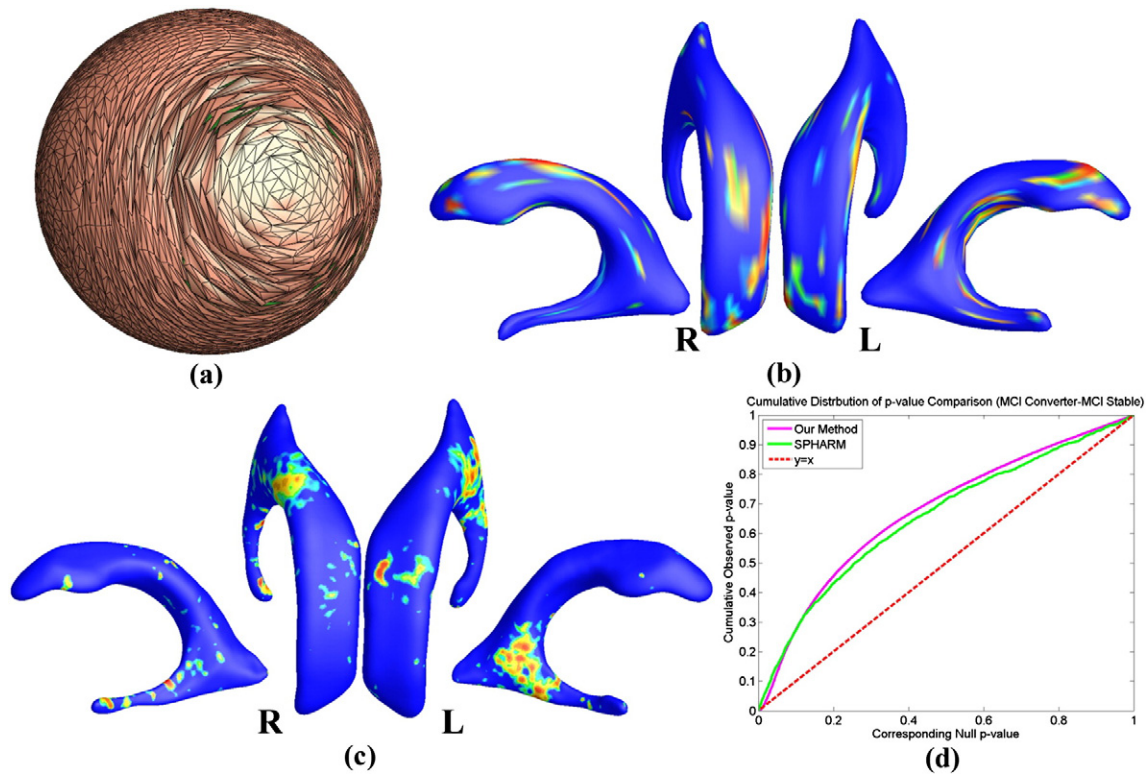

Fig. 10. Comparison with SPHARM. (a) is the spherical harmonic mapping of a left ventricular surface; (b) is the statistical map from SPHARM (Styner et al., 2006) showing local shape differences (*p*-values) between MCI converter (N = 58) and MCI stable (N = 53) groups from the ADNI baseline dataset; (c) is the statistical map from our method showing local shape differences (*p*-values) between the same groups as in (b); (d) shows the CDF plots comparing the two methods.

comparison of the resulting *p*-values for each method. While the line $y = x$ represents null hypothesis, which implies there is no detectable difference, a steeper curve suggests that greater differences are detected. The details of the experiment with SPHARM can be found in (Shi et al., 2013a). From the CDF comparison, both methods got comparable results, but our method is more robust for processing the concave ventricular surfaces. The inferior horn on the lateral ventricle is also important for the study of AD, as it is adjacent to the hippocampus and its enlargement may indicate hippocampal atrophy—a well-established biomarker for AD. As shown in Fig. 6, our approach detected significant differences on both left and right inferior horns. Even with a small dataset, our method detected significant differences on the right inferior horn, as shown in Fig. 10(c). The significance *p*-maps of the two methods are not quite consistent, most probably because that details in the original image segmentations were greatly removed during the resolution resampling step of SPHARM. A more convincing way to validate the new algorithm is to apply it to study cortical surface morphometry and compare the results to other extensively applied cortical analysis tools such as FreeSurfer (Fischl et al., 1999a). We will address this problem in future work.

Comparisons with voxel-based morphometry and pattern analysis

When studying brain morphology with imaging, the voxel-based morphometry (VBM) method has been extensively developed, improved, and used (Ashburner and Friston, 2000; Good et al., 2001; Killgore et al., 2012; Mechelli et al., 2005; Niedtfeld I et al., 2013; Whitwell, 2009). Briefly, VBM starts by spatially normalizing the T1-weighted image of each individual subject to a template image to establish a voxel-to-voxel correspondence across subjects. The registration process consists of both affine transformation and a nonlinear deformation. After segmenting the registered images into tissue classes, each voxel contains a measure of the probability that it belongs to a specific segmentation class. This quantity can be used to compute other brain anatomical features such as gray matter volume (Ashburner and Friston, 2000). Voxel-wise statistical analyses are then applied to study local differences in the anatomical features of each tissue class across subjects. The VBM method is available in many major neuro-imaging software packages such as FSL and SPM and is efficient and easy to apply. However, the VBM method may have limited accuracy in measuring some aspects of brain morphology, particularly in regions where fine anatomical features are found within brain structures. For example, the cerebral cortex has a highly folded geometry. Many of its anatomical features are built in deep folds. The voxel-wise nature of the VBM method may limit its capability to accurately measure such features and to align these features across subjects. On the other hand, our surface-based method can achieve sub-voxel accuracy when applied to some specific structures. For example, as discussed above, the hyperbolic Ricci flow method can conformally flatten a convoluted cortical surface onto a 2D domain (Shi et al., 2013c). The flattened cortical surface retains substantial geometric information about the original surface with no singularities or overlap in the mapping, so all features in the cortical folds are well preserved and can be accurately analyzed. Pattern analysis (Joshi et al., 2011; Li et al., 2010; Liu et al., 2014) is another commonly applied method, which aims to identify the most discriminative disease-related features in brain images or surfaces. In this paper, the proposed method is based on tensor-based morphometry (TBM), which is generalized to deal with 3D surfaces, to study the morphological deformation patterns of ventricular surfaces along with disease progression. The TBM features encode rich information about the local surface geometry, which may be inaccessible or overlooked in other methods (Chung et al., 2008, 2003b; Davatzikos, 1996; Thompson et al., 2000). Experimental results in our group difference study illustrate the differentiation power of the TBM features, as shown in Fig. 6. These TBM features may also improve MRI-based diagnostic classification with sparse learning based feature selection method (Wang et al., 2013b). Despite the many advantages of the proposed method, however, a few issues need to be addressed before it can be established as an attractive alternative to other methods. First, more experiments on large-scale datasets of ventricular and other brain structure surfaces, especially cortical surfaces, are necessary to validate the efficacy of the method. Second, the system needs to be automated to hide the complex details for general users. Third, the ability of TBM features in diagnostic classification needs more systematic study. We will address these problems in our future work.

Statistical feature smoothing

In our surface processing pipeline, each of the MR image acquisition, image segmentation, surface reconstruction, surface parameterization, and surface registration procedures is expected to introduce noise in the TBM statistical features. The mesh smoothing process introduced in Section Image acquisition and preprocessing is used to reduce the noise from image acquisition, segmentation and partial volume effects in surface reconstruction (Shi et al., 2013a). The remaining noise and noise introduced in subsequent processes still affect the SNR in the TBM features and the final statistical analysis. Thus, we have applied the heat kernel smoothing algorithm (Chung et al., 2005b) to the TBM features before the group difference and correlation studies, as introduced in Section Surface tensor-based morphometry and its smoothness with heat kernel method. From Eq. (14), the bandwidth of the smoothing process is determined by the number of iterations. As pointed out in (Han et al., 2006), the correlation of noise in surface measurements falls off rapidly with distance on the surface, so it is sufficient to use a small kernel bandwidth. For heat kernel smoothing on cortical surfaces, usually applied parameters include bandwidth $\sigma = 1$ and number of iterations $m = 200$ yielding the effective smoothness of $\sqrt{m} = 14.14$ mm (Chung et al., 2005a) or even smaller smoothness values such as 6 mm in (Han et al., 2006). Based on these observations, in our experiment, we set $\sigma = 1$, $m = 10$ giving the effective smoothness of 3.16 mm. As few studies in the literature have validated the performance of the heat kernel smoothing method (Seo et al., 2010), the smoothing parameters were chosen tentatively. The group difference *p*-map with unsmoothed TBM features is shown in Fig. 11. In Fig. 6, the significant areas are consistent with those in Fig. 11, but the noisy distributions are greatly improved by the smoothing process. Similar comparison studies for correlation-based *p*-maps give similar results. Thus the parameters are suitable for our current studies. A potential future work is to quantitatively study the effects of the heat kernel smoothing process on the statistical analysis.

Surface multivariate tensor-based morphometry

In some of our prior studies (Wang et al., 2013b, 2010), the multivariate tensor-based morphometry (mTBM) was proved to be more powerful for checking group differences than other statistics including TBM. This paper used TBM as the statistic instead of mTBM because for the lateral ventricle, a fluid-filled subcortical structure, its changes vary drastically with normal aging, disease progression, or other brain activities. As the mTBM is very sensitive to local changes, the resulting significantly different areas spread on the ventricular surface even after smoothing, making the results difficult to be interpreted as meaningful anatomical findings or noise from subtle changes. Thus here we used TBM as the measurement of changes.

Integration of relative pose statistical analysis

In the current study, the proposed surface-based ventricular morphometry system relies on shape changes of the lateral ventricles along with disease progression. Similar to other shape analysis studies of a single structure, ventricular pose information is discarded in our
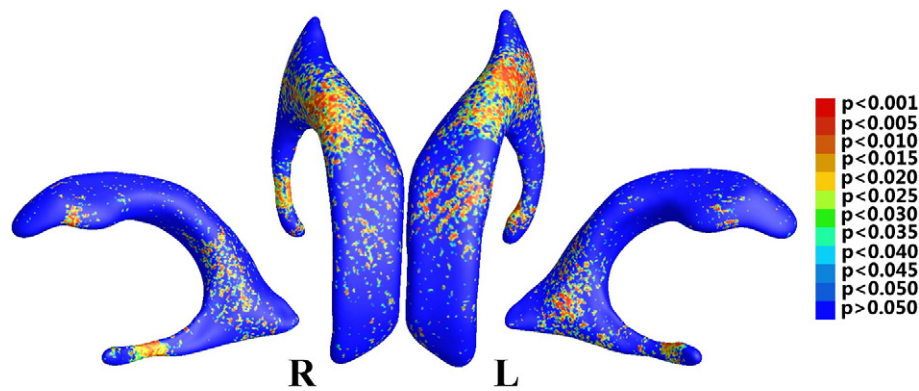
Fig. 11. Illustration of statistical map showing local shape differences (*p*-values) between MCI converter and MCI stable groups from the ADNI baseline dataset, based on determinant of Jacobian matrix (TBM), which was not smoothed.

system during the surface registration stage. Pose mainly depends on extrinsic factors such as the position and orientation of a ventricular surface in $\mathbb{R}^3$ while our method depends on the intrinsic factors of the ventricular surfaces such as local enlargement. Although it rarely happens that atrophy of brain tissue causes only pose changes in adjacent structures without any local shape deformation, pose information is still very important in brain morphometry studies. In (Bossa et al., 2011), the statistical analysis of relative pose was presented to study brain atrophy associated pose changes of the subcortical nuclei in AD. Same method was applied in (Lao et al., 2013) to study pose changes of thalamus due to prematurity and in (Lao et al., 2014) to study pose changes of corpus callosum due to traumatic brain injury. Briefly, the relative pose is computed by following steps, where we take ventricular surfaces as an example. First, one-to-one point correspondences between different ventricular surfaces are established by a surface registration algorithm, such as the method proposed in this paper. Second, for each registered ventricular surface, a pose matrix is obtained by fitting a template shape to this surface with a Procrustes alignment. Third, the mean pose is calculated iteratively with the pose matrix of each ventricular surface. The relative pose of each ventricular surface, which consists of 7 parameters: 1 scale scalar, 3 rotation scalars and 3 translation scalars, is obtained by subtracting the mean pose from its pose matrix. Statistical analyses are then applied on the relative pose parameters. For details of the algorithm, please refer to (Bossa et al., 2011). Since our ventricular surface analysis gives indirect information about the atrophy of surrounding brain structures, integration of relative pose analysis in our system may help to better understand the abnormal growth of brain tissue adjacent to lateral ventricles. In future, we will try to integrate the statistical analysis of relative pose information in our system.

In neuroimaging research, T1-weighted MRI has high contrast differences from surrounding structures making accurate lateral ventricle segmentation straightforward for both manual and automatic methods (Carmichael et al., 2007; Chou et al., 2010; Ferrarini et al., 2006; Jack et al., 2003; Thompson et al., 2004a). Thus structural MRI based lateral ventricular structure has been used to study a variety of human diseases including AD (Chou et al., 2009a; Ferrarini et al., 2006, 2008a; Gutman et al., 2013; Jack et al., 2003; Thompson et al., 2004a; Wang et al., 2011), HIV/AIDS (Thompson et al., 2006; Wang et al., 2010), normal pressure hydrocephalus (Bader et al., 2013), ventriculomegaly (Paniagua et al., 2013), vascular dementia (Bader et al., 2013), diabetes mellitus (Lee et al., 2013), drug addiction (Jeong et al., 2013), and others. Our proposed algorithm is very generalizable and may be applied to a similar range of diseases including but not limited to AD. Starting from our prior work on brain surface conformal parameterization (Gu et al., 2004; Shi et al., 2013c, 2013d; Wang et al., 2009b, 2009c, 2007), here we show that the hyperbolic Ricci flow method can be adopted to analyze branching ventricular morphometry. Besides its

global non-singularity parameterization, our method also carries a few other novel ideas, such as using geodesic curve lifting to enforce a meaningful boundary matching, diffeomorphic surface registration via the Klein model, and combing hyperbolic conformal parameterization with TBM analysis. We expect that our work can provide some practical experience and inspire more interest in hyperbolic geometry related neuroimaging research.

Conclusion

In this paper, we present a hyperbolic Ricci flow and surface TBM based ventricular morphometry system, which can improve the computational efficiency and accuracy for in vivo regional structural MRI lateral ventricle estimation. Our approach introduces the hyperbolic Ricci flow method which computes a ventricular surface conformal parameterization on the hyperbolic Poincaré disk without any singularity. Through geodesic curve lifting and the conversion to the Klein model (Zeng et al., 2010), we can compute a diffeomorphic surface mapping with consistent boundary matching condition. Furthermore, we compute the TBM from the well-organized conformal grids and use it to capture any possible subtle surface deformations. We applied the developed tool to our ongoing work on MCI conversion prediction (Chen et al., 2013) and our results demonstrated that our proposed method achieved good correlation with cognition and other AD biomarker such as FDG-PET, which may help predict longitudinal AD conversion by capturing subtle ventricular morphometric differences from the baseline image analysis.

In the past few years, our group has developed a series of structural MRI analysis software tools for AD research, such as multivariate TBM on cortical surface (Wang et al., 2013b) and hippocampal abnormality analyses (Shi et al., 2014, 2013a, 2013b; Wang et al., 2011), together with cortical thickness estimation with volumetric Laplace–Beltrami operator and heat kernel (Wang et al., 2013a, 2014). In the future, we plan to apply our structural MRI software tools in our ongoing preclinical AD research (Caselli and Reiman, 2013; Langbaum et al., 2013). We will carefully explore a broad range of research questions on structural MRI analysis (Braskie and Thompson, 2014), such as (1) structural MRI as an AD biomarker to measure AD progression; (2) the relationship of structural MRI to cognition (3) and to other AD biomarkers including amyloid imaging and FDG-PET, and (4) the value for structural MRI measures to help predict cognitive decline.

References

Alhadidi, A., Cevidanes, L.H., Paniagua, B., Cook, R., Festy, F., Tyndall, D., 2012. 3D quantification of mandibular asymmetry using the SPHARM-PDM tool box. Int. J. Comput. Assist. Radiol. Surg. 7, 265–271.

Apostolova, L.G., Mosconi, L., Thompson, P.M., Green, A.E., Hwang, K.S., Ramirez, A., Mistur, R., Tsui, W.H., de Leon, M.J., 2010a. Subregional hippocampal atrophy predicts Alzheimer's dementia in the cognitively normal. Neurobiol. Aging 31, 1077–1088.

Apostolova, L.G., Thompson, P.M., Green, A.E., Hwang, K.S., Zoumalan, C., Jack Jr., C.R., Harvey, D.J., Petersen, R.C., Thal, L.J., Aisen, P.S., Toga, A.W., Cummings, J.L., Decarli, C.S., 2010b. 3D comparison of low, intermediate, and advanced hippocampal atrophy in MCI. Hum. Brain Mapp. 31, 786–797.

Ashburner, J., Friston, K.J., 2000. Voxel-based morphometry—the methods. Neuroimage 11, 805–821.

Auzias, G., Lefevre, J., Le Troter, A., Fischer, C., Perrot, M., Regis, J., Coulon, O., 2013. Model-driven harmonic parameterization of the cortical surface: HIP-HOP. IEEE Trans. Med. Imaging 32, 873–887.

Bader, C., Cyrille, C., Jadwiga, Z., Joel, D., Fichten, A., Catherine, G.J., Roger, B., Olivier, B., 2013. Estimation of the lateral ventricles volumes from a 2D image and its relationship with cerebrospinal fluid flow. Biomed. Res. Int. 2013, 215989.

Bakircioglu, M., Joshi, S., Miller, M.I., 1999. Landmark matching on brain surfaces via large deformation diffeomorphisms on the sphere. Proc. SPIE Medical Imaging, pp. 710–715.

Bossa, M., Zacur, E., Olmos, S., 2011. Statistical analysis of relative pose information of subcortical nuclei: application on ADNI data. Neuroimage 55, 999–1008.

Braak, H., Alafuzoff, I., Arzberger, T., Kretzschmar, H., Del Tredici, K., 2006. Staging of Alzheimer disease-associated neurofibrillary pathology using paraffin sections and immunocytochemistry. Acta Neuropathol. 112, 389–404.

Braskie, M.N., Thompson, P.M., 2014. A focus on structural brain imaging in the Alzheimer's disease neuroimaging initiative. Biol. Psychiatry 75, 527–533.

Buckner, R.L., Andrews-Hanna, J.R., Schacter, D.L., 2008. The brain's default network: anatomy, function, and relevance to disease. Ann. N. Y. Acad. Sci. 1124, 1–38.

Cardenas, V.A., Chao, L.L., Studholme, C., Yaffe, K., Miller, B.L., Madison, C., Buckley, S.T., Mungas, D., Schuff, N., Weiner, M.W., 2011. Brain atrophy associated with baseline and longitudinal measures of cognition. Neurobiol. Aging 32, 572–580.

Carmichael, O.T., Kuller, L.H., Lopez, O.L., Thompson, P.M., Dutton, R.A., Lu, A., Lee, S.E., Lee, J.Y., Aizenstein, H.J., Meltzer, C.C., Liu, Y., Toga, A.W., Becker, J.T., 2007. Ventricular volume and dementia progression in the Cardiovascular Health Study. Neurobiol. Aging 28, 389–397.

Caroli, A., Prestia, A., Chen, K., Ayutyanont, N., Landau, S.M., Madison, C.M., Haense, C., Herholz, K., Nobili, F., Reiman, E.M., Jagust, W.J., Frisoni, G.B., 2012. Summary metrics to assess Alzheimer disease-related hypometabolic pattern with 18 F-FDG PET: head-to-head comparison. J. Nucl. Med. 53, 592–600.

Caselli, R.J., Reiman, E.M., 2013. Characterizing the preclinical stages of Alzheimer's disease and the prospect of presymptomatic intervention. J. Alzheimers Dis. 33 (Suppl. 1), S405–S416.

Chen, K., Reiman, E.M., Alexander, G.E., Caselli, R.J., Gerkin, R., Bandy, D., Domb, A., Osborne, D., Fox, N., Crum, W.R., Saunders, A.M., Hardy, J., 2007. Correlations between apolipoprotein E epsilon4 gene dose and whole brain atrophy rates. Am. J. Psychiatry 164, 916–921.

Chen, K., Ayutyanont, N., Langbaum, J.B.S., Fleisher, A.S., Reschke, C., Lee, W., Liu, X., Bandy, D., Alexander, G.E., Thompson, P.M., Shaw, L., Trojanowski, J.Q., Jack Jr., C.R., Landau, S.M., Foster, N.L., Harvey, D.J., Weiner, M.W., Koeppe, R.A., Jagust, W.J., Reiman, E.M., 2011. Characterizing Alzheimer's disease using a hypometabolic convergence index. Neuroimage 56, 52–60.

Chen, K., Ayutyanont, N., Langbaum, J.B., Fleisher, A.S., Reschke, C., Lee, W., Liu, X., Alexander, G.E., Bandy, D., Caselli, R.J., Reiman, E.M., 2012. Correlations between FDG PET glucose uptake-MRI gray matter volume scores and apolipoprotein E epsilon4 gene dose in cognitively normal adults: a cross-validation study using voxel-based multi-modal partial least squares. Neuroimage 60, 2316–2322.

Chen, K., Stonnington, C., Ayutyanont, N., Reschke, C., Thiyyagura, P., Protas, H., Liu, X., Roontiva, A., Parks, S., Bauer, R., Lee, W., Fleisher, A., Reiman, E., 2013. Baseline FDG PET and volumetric MRI predicts Alzheimer's disease conversion from mild cognitive impairment: An ADNI study. Alzheimer's Association International Conference, Boston.

Chou, Y.-Y., Leporé, N., Avedissian, C., Madsen, S.K., Parikshak, N., Hua, X., Shaw, L.M., Trojanowski, J.Q., Weiner, M.W., Toga, A.W., Thompson, P.M., 2009a. Mapping correlations between ventricular expansion and CSF amyloid and tau biomarkers in 240 subjects with Alzheimer's disease, mild cognitive impairment and elderly controls. Neuroimage 46, 394–410.

Chou, Y.-Y., Leporé, N., Chiang, M., Avedissian, C., Barysheva, M., McMahon, K.L., de Zubicaray, G.I., Meredith, M., Wright, M.J., Toga, A.W., Thompson, P.M., 2009b. Mapping genetic influences on ventricular structure in twins. Neuroimage 44, 1312–1323.

Chou, Y.-Y., Leporé, N., Saharan, P., Madsen, S.K., Hua, X., Jack, C.R., Shaw, L.M., Trojanowski, J.Q., Weiner, M.W., Toga, A.W., Thompson, P.M., 2010. Ventricular maps in 804 ADNI subjects: correlations with CSF biomarkers and clinical decline. Neurobiol. Aging 31, 1386–1400.

Chung, M.K., Worsley, K.J., Robbins, S., Evans, A.C., 2003a. Tensor-based brain surface modeling and analysis. IEEE Conference on Computer Vision and Pattern Recognition, pp. 467–473.

Chung, M.K., Worsley, K.J., Robbins, S., Paus, T., Taylor, J., Giedd, J.N., Rapoport, J.L., Evans, A.C., 2003b. Deformation-based surface morphometry applied to gray matter deformation. Neuroimage 18, 198–213.

Chung, M.K., Robbins, S., Evans, A.C., 2005a. Unified statistical approach to cortical thickness analysis. Information Processing in Medical Imaging (IPMI), pp. 627–638.

Chung, M.K., Robbins, S.M., Dalton, K.M., Davidson, R.J., Alexander, A.L., Evans, A.C., 2005b. Cortical thickness analysis in autism with heat kernel smoothing. Neuroimage 25, 1256–1265.

Chung, M.K., Dalton, K.M., Davidson, R.J., 2008. Tensor-based cortical surface morphometry via weighted spherical harmonic representation. IEEE Trans. Med. Imaging 27, 1143–1151.

Collins, D.L., Neelin, P., Peters, T.M., Evans, A.C., 1994. Automatic 3D intersubject registration of MR volumetric data in standardized Talairach space. J. Comput. Assist. Tomogr. 18, 192–205.

Colom, R., Stein, J.L., Rajagopalan, P., Martínez, K., Hermel, D., Wang, Y., Álvarez-Linera, J., Burgaleta, M., Quiroga, M.A., Shih, P.C., Thompson, P.M., 2013. Hippocampal structure and human cognition: key role of spatial processing and evidence supporting the efficiency hypothesis in females. Intelligence 41, 129–140.

Costafreda, S.G., Dinov, I.D., Tu, Z., Shi, Y., Liu, C.Y., Kloszewska, I., Mecocci, P., Soininen, H., Tsolaki, M., Vellas, B., Wahlund, L.O., Spenger, C., Toga, A.W., Lovestone, S., Simmons, A., 2011. Automated hippocampal shape analysis predicts the onset of dementia in mild cognitive impairment. Neuroimage 56, 212–219.

Davatzikos, C., 1996. Spatial normalization of 3D brain images using deformable models. J. Comput. Assist. Tomogr. 20, 656–665.

den Heijer, T., van der Lijn, F., Koudstaal, P.J., Hofman, A., van der Lugt, A., Krestin, G.P., Niessen, W.J., Breteler, M.M.B., 2010. A 10-year follow-up of hippocampal volume on magnetic resonance imaging in early dementia and cognitive decline. Brain 133, 1163–1172.

Dewey, J., Hana, G., Russell, T., Price, J., McCaffrey, D., Harezlak, J., Sem, E., Anyanwu, J.C., Guttmann, C.R., Navia, B., Cohen, R., Tate, D.F., 2010. Reliability and validity of MRI-based automated volumetry software relative to auto-assisted manual measurement of subcortical structures in HIV-infected patients from a multisite study. Neuroimage 51, 1334–1344.

Do Carmo, M.P., 1976. Differential Geometry of Curves and Surfaces. Prentice-Hall, Inc.

Ferrarini, L., Palm, W.M., Olofsen, H., van Buchem, M.A., Reiber, J.H.C., Admiraal-Behloul, F., 2006. Shape differences of the brain ventricles in Alzheimer's disease. Neuroimage 32, 1060–1069.

Ferrarini, L., Palm, W.M., Olofsen, H., van der Landen, R., Blauw, G.J., Westendorp, R.G.J., Bollen, E.L.E.M., Middelkoop, H.A.M., Reiber, J.H.C., van Buchem, M.A., Admiraal-Behloul, F., 2008a. MMSE scores correlate with local ventricular enlargement in the spectrum from cognitively normal to Alzheimer disease. Neuroimage 39, 1832–1838.

Ferrarini, L., Palm, W.M., Olofsen, H., van der Landen, R., van Buchem, M.A., Reiber, J.H.C., Admiraal-Behloul, F., 2008b. Ventricular shape biomarkers for Alzheimer's disease in clinical MR images. Magn. Reson. Med. 59, 260–267.

Fischl, B., Sereno, M.I., Dale, A.M., 1999a. Cortical surface-based analysis II: Inflation, flattening, and a surface-based coordinate system. Neuroimage 9, 195–207.

Fischl, B., Sereno, M.I., Tootell, R.B., Dale, A.M., 1999b. High-resolution intersubject averaging and a coordinate system for the cortical surface. Hum. Brain Mapp. 8, 272–284.

Folstein, M.F., Folstein, S.E., McHugh, P.R., 1975. "Mini-mental state". A practical method for grading the cognitive state of patients for the clinician. J. Psychiatr. Res. 12, 189–198.

Fox, N.C., Scahill, R.I., Crum, W.R., Rossor, M.N., 1999. Correlation between rates of brain atrophy and cognitive decline in AD. Neurology 52, 1687–1689.

Frisoni, G.B., Fox, N.C., Jack, C.R., Scheltens, P., Thompson, P.M., 2010. The clinical use of structural MRI in Alzheimer disease. Nat. Rev. Neurol. 6, 67–77.

Gauthier, S., Reisberg, B., Zaudig, M., Petersen, R.C., Ritchie, K., Broich, K., Belleville, S., Brodaty, H., Bennett, D., Chertkow, H., Cummings, J.L., de Leon, M., Feldman, H., Ganguli, M., Hampel, H., Scheltens, P., Tierney, M.C., Whitehouse, P., Winblad, B., 2006. Mild cognitive impairment. Lancet 367, 1262–1270.

Gerig, G., Styner, M., Jones, D., Weinberger, D., Lieberman, M., 2001. Shape analysis of brain ventricles using SPHARM. IEEE Workshop on Mathematical Methods in Biomedical Image, Analysis (MMBIA'01).

Good, C.D., Johnsrude, I., Ashburner, J., H., R.N., Friston, K.J., Frackowiak, R.S., 2001. Cerebral asymmetry and the effects of sex and handedness on brain structure: a voxel-based morphometric analysis of 465 normal adult human brains. Neuroimage 14, 685–700.

Gu, X., Yau, S.-T., 2008. Computational Conformal Geometry. International Press of Boston.

Gu, X., Wang, Y., Chan, T.F., Thompson, P.M., Yau, S.-T., 2004. Genus zero surface conformal mapping and its application to brain surface mapping. IEEE Trans. Med. Imaging 23, 949–958.

Gutman, B.A., Hua, X., Rajagopalan, P., Chou, Y.Y., Wang, Y., Yanovsky, I., Toga, A.W., Jack Jr., C.R., Weiner, M.W., Thompson, P.M., 2013. Maximizing power to track Alzheimer's disease and MCI progression by LDA-based weighting of longitudinal ventricular surface features. Neuroimage 70, 386–401.

Hamilton, R.S., 1988. The Ricci flow on surfaces. Contemp. Math. 71, 237–262.

Han, X., Xu, C., Prince, J.L., 2003. A topology preserving level set method for geometric deformable models. IEEE Trans. Pattern Anal. Mach. Intell. 25, 755–768.

Han, X., Jovicich, J., Salat, D., Kouwe, A.v.d. Quinn, B., Czanner, S., Busa, E., Pacheco, J., Albert, M., Killiany, R., Maguire, P., Rosas, D., Makris, N., Dale, A., Dickerson, B., Fischl, B., 2006. Reliability of MRI-derived measurements of human cerebral cortical thickness: the effects of field strength, scanner upgrade and manufacturer. Neuroimage 32, 180–194.

Henneman, W.J., Vrenken, H., Barnes, J., Sluimer, I.C., Verwey, N.A., Blankenstein, M.A., Klein, M., Fox, N.C., Scheltens, P., Barkhof, F., van der Flier, W.M., 2009. Baseline CSF p-tau levels independently predict progression of hippocampal atrophy in Alzheimer disease. Neurology 73, 935–940.

Holland, D., Brewer, J.B., Hagler, D.J., Fenema-Notestine, C., Dale, A.M., 2009. Subregional neuroanatomical change as a biomarker for Alzheimer's disease. Proc. Natl. Acad. Sci. U. S. A. 106, 20954–20959.

Hoppe, H., 1996. Progressive meshes. Proceedings of the 23rd Annual Conference on Computer Graphics and Interactive Techniques. ACM, pp. 99–108.

Hua, X., Lee, S., Hibar, D.P., Yanovsky, I., Leow, A.D., Toga, A.W., Jack Jr., C.R., Bernstein, M.A., Reiman, E.M., Harvey, D.J., Kornak, J., Schuff, N., Alexander, G.E., Weiner, M.W., Thompson, P.M., 2010. Mapping Alzheimer's disease progression in 1309 MRI scans: power estimates for different inter-scan intervals. Neuroimage 51, 63–75.

Hua, X., Gutman, B., Boyle, C., Rajagopalan, P., Leow, A.D., Yanovsky, I., Kumar, A.R., Toga, A.W., Jack Jr., C.R., Schuff, N., Alexander, G.E., Chen, K., Reiman, E.M., Weiner, M.W., Thompson, P.M., 2011. Accurate measurement of brain changes in longitudinal MRI scans using tensor-based morphometry. Neuroimage 57, 5–14.

Hurdal, M.K., Stephenson, K., 2004. Cortical cartography using the discrete conformal approach of circle packings. Neuroimage 23, S119–S128.

Hurdal, M.K., Stephenson, K., 2009. Discrete conformal methods for cortical brain flattening. Neuroimage 45, S86–S98.

Hyman, B.T., 2011. Amyloid-dependent and amyloid-independent stages of Alzheimer disease. Arch. Neurol. 68, 1062–1064.

ICD, 2010. Mild cognitive impairment, so stated. ICD-9-CM Index to Diseases and Injuries (FY10) [online]Available from ftp://ftp.cdc.gov/pub/Health_Statistics/ NCHS/Publications/ICD9-CM/2009/.

Jack Jr., C.R., Slomkowski, M., Gracon, S., Hoover, T.M., Felmlee, J.P., Stewart, K., Xu, Y., Shiung, M., O'Brien, P.C., Cha, R., Knopman, D., Petersen, R.C., 2003. MRI as a biomarker of disease progression in a therapeutic trial of milameline for AD. Neurology 60, 253–260.

Jack Jr., C.R., Shiung, M.M., Gunter, J.L., O'Brien, P.C., Weigand, S.D., Knopman, D.S., Boeve, B.F., Ivnik, R.J., Smith, G.E., Cha, R.H., Tangalos, E.G., Petersen, R.C., 2004. Comparison of different MRI brain atrophy rate measures with clinical disease progression in AD. Neurology 62, 591–600.

Jack Jr., C.R., Weigand, S.D., Shiung, M.M., Przybelski, S.A., O'Brien, P.C., Gunter, J.L., Knopman, D.S., Boeve, B.F., Smith, G.E., Petersen, R.C., 2008. Atrophy rates accelerate in amnestic mild cognitive impairment. Neurology 70, 1740–1752.

Jack Jr., C.R., Lowe, V.J., Weigand, S.D., Wiste, H.J., Senjem, M.L., Knopman, D.S., Shiung, M.M., Gunter, J.L., Boeve, B.F., Kemp, B.J., Weiner, M., Petersen, R.C., 2009. Serial PIB and MRI in normal, mild cognitive impairment and Alzheimer's disease: implications for sequence of pathological events in Alzheimer's disease. Brain 132, 1355–1365.

Jack Jr., C.R., Wiste, H.J., Vemuri, P., Weigand, S.D., Senjem, M.L., Zeng, G., Bernstein, M.A., Gunter, J.L., Pankratz, V.S., Aisen, P.S., Weiner, M.W., Petersen, R.C., Shaw, L.M., Trojanowski, J.Q., Knopman, D.S., 2010. Brain beta-amyloid measures and magnetic resonance imaging atrophy both predict time-to-progression from mild cognitive impairment to Alzheimer's disease. Brain 133, 3336–3348.

Jeong, H.S., Lee, S., Yoon, S., Jung, J.J., Cho, H.B., Kim, B.N., Ma, J., Ko, E., Im, J.J., Ban, S., Renshaw, P.F., Lyoo, I.K., 2013. Morphometric abnormalities of the lateral ventricles in methamphetamine-dependent subjects. Drug Alcohol Depend. 131, 222–229.

Jin, M., Kim, J., Luo, F., Gu, X., 2008. Discrete surface Ricci flow. IEEE Trans. Vis. Comput. Graph. 14, 1030–1043.

Joshi, A.A., Shattuck, D.W., Thompson, P.M., Leahy, R.M., 2007. Surface-constrained volumetric brain registration using harmonic mappings. IEEE Trans. Med. Imaging 26, 1657–1669.

Joshi, S.H., Bowman, I., Toga, A.W., Van Horn, J.D., 2011. Brain pattern analysis of cortical valued distributions. IEEE International Symposium on Biomedical Imaging: from nano to macro,pp. 1117–1120.

Killgore, W.D.S., Schwab, Z.J., Kipman, M., DelDonno, S.R., Weber, M., 2012. Voxel-based morphometric gray matter correlates of daytime sleepiness. Neurosci. Lett. 518, 10–13.

Kremen, W.S., Panizzon, M.S., Neale, M.C., Fennema-Notestine, C., Prom-Wormley, E., Eyler, L.T., Stevens, A., Franz, C.E., Lyons, M.J., Grant, M.D., Jak, A.J., Jernigan, T.L., Xian, H., Fischl, B., Thermenos, H.W., Seidman, L.J., Tsuang, M.T., Dale, A.M., 2012. Heritability of brain ventricle volume: converging evidence from inconsistent results. Neurobiol. Aging 33, 1–8.

Langbaum, J.B., Fleisher, A.S., Chen, K., Ayutyanont, N., Lopera, F., Quiroz, Y.T., Caselli, R.J., Tariot, P.N., Reiman, E.M., 2013. Ushering in the study and treatment of preclinical Alzheimer disease. Nat. Rev. Neurol. 9, 371–381.

Lao, Y., Shi, J., Wang, Y., Ceschin, R., Hwang, D., Nelson, M.D., Panigrahy, A., Leporé, N., 2013. Statistical Analysis of Relative Pose of the Thalamus in Preterm Neonates. MICCAI workshop on CLinical Imagebased Procedures (CLIP 2013): Translational Research in Medical Imaging, pp. 1–9.

Lao, Y., Gajawelli, N., Hass, L., Wilkins, B., Hwang, D., Tsao, S., Wang, Y., Law, M., Leporé, N., 2014. 3D pre- versus post-season comparisons of surface and relative pose of the corpus callosum in contact sport athletes. SPIE Med. Imaging 9034. http://dx.doi.org/10.1117/12.2043245.

Lee, J.H., Yoon, S., Renshaw, P.F., Kim, T.S., Jung, J.J., Choi, Y., Kim, B.N., Jacobson, A.M., Lyoo, I.K., 2013. Morphometric changes in lateral ventricles of patients with recent-onset type 2 diabetes mellitus. PLoS One 8, e60515.

Leech, R., Sharp, D.J., 2014. The role of the posterior cingulate cortex in cognition and disease. Brain 137, 12–32.

Leow, A.D., Yanovsky, I., Parikshak, N., Hua, X., Lee, S., Toga, A.W., Jack Jr., C.R., Bernstein, M.A., Britson, P.J., Gunter, J.L., Ward, C.P., Borowski, B., Shaw, L.M., Trojanowski, J.Q., Fleisher, A.S., Harvey, D., Kornak, J., Schuff, N., Alexander, G.E., Weiner, M.W., Thompson, P.M., 2009. Alzheimer's disease neuroimaging initiative: a one-year follow up study using tensor-based morphometry correlating degenerative rates, biomarkers and cognition. Neuroimage 45, 645–655.

Li, K., Guo, L., Li, G., Nie, J., Faraco, C., Cui, G., Zhao, Q., Miller, L.S., Liu, T., 2010. Gyral folding pattern analysis via surface profiling. Neuroimage 52, 1202–1214.

Li, Y., Wang, Y., Wu, G., Shi, F., Zhou, L., Lin, W., Shen, D., 2012. Discriminant analysis of longitudinal cortical thickness changes in Alzheimer's disease using dynamic and network features. Neurobiol. Aging 33 (427), e415–e430.

Liu, S., Cai, W., Wen, L., Feng, D.D., Pujol, S., Kikinis, R., Fulham, M.J., Eberl, S., 2014. Multichannel neurodegenerative pattern analysis and its application in Alzheimer's disease characterization. Comput. Med. Imaging Graph. 38 (6), 436–444.

Loop, C., 1987. Smooth Subdivision Surfaces Based on Triangles. Mathematics Department. University of Utah.

Lorensen, W.E., Cline, H.E., 1987. Marching cubes: a high resolution 3D surface construction algorithm. SIGGRAPH Comput. Graph 21, pp. 163–169.

Luders, E., Thompson, P.M., Kurth, F., Hong, J.Y., Phillips, O.R., Wang, Y., Gutman, B.A., Chou, Y.Y., Narr, K.L., Toga, A.W., 2013. Global and regional alterations of hippocampal anatomy in long-term meditation practitioners. Hum. Brain Mapp. 34, 3369–3375.

Luo, F., Gu, X., Dai, J., 2008. Variational Principles on Discrete Surfaces. International Press.

Madsen, S.K., Ho, A.J., Hua, X., Saharan, P.S., Toga, A.W., Jack Jr., C.R., Weiner, M.W., Thompson, P.M., 2010. 3D maps localize caudate nucleus atrophy in 400 AD, MCI, and healthy subjects. Neurobiol. Aging 31, 1312–1325.

Matsuda, H., 2007a. Role of neuroimaging in Alzheimer's disease, with emphasis on brain perfusion SPECT. J. Nucl. Med. 48, 1289–1300.

Matsuda, H., 2007b. The role of neuroimaging in mild cognitive impairment. Neuropathology 27, 570–577.

McEvoy, L.K., Fennema-Notestine, C., Roddey, J.C., Hagler Jr., D.J., Holland, D., Karow, D.S., Pung, C.J., Brewer, J.B., Dale, A.M., 2009. Alzheimer disease: quantitative structural neuroimaging for detection and prediction of clinical and structural changes in mild cognitive impairment. Radiology 251, 195–205.

Mechelli, A., Price, C.J., Friston, K.J., Ashburner, J., 2005. Voxel-based morphometry of the human brain: methods and applications. Curr. Med. Imaging Rev. 1, 105.

Monje, M., Thomason, M.E., Rigolo, L., Wang, Y., Waber, D.P., Sallan, S.E., Golby, A.J., 2013. Functional and structural differences in the hippocampus associated with memory deficits in adult survivors of acute lymphoblastic leukemia. Pediatr. Blood Cancer 60, 293–300.

Morra, J.H., Tu, Z., Apostolova, L.G., Green, A.E., Avedissian, C., Madsen, S.K., Parikshak, N., Toga, A.W., Jack Jr., C.R., Schuff, N., Weiner, M.W., Thompson, P.M., 2009. Automated mapping of hippocampal atrophy in 1-year repeat MRI data from 490 subjects with Alzheimer's disease, mild cognitive impairment, and elderly controls. Neuroimage 45, S3–S15.

Nichols, T.E., Holmes, A.P., 2002. Nonparametric permutation tests for functional neuroimaging: a primer with examples. Hum. Brain Mapp. 15, 1–25.

Niedtfeld I, I., Schulze, L., Krause-Utz, A., Demirakca, T., Bohus, M., Schmahl, C., 2013. Voxel-based morphometry in women with borderline personality disorder with and without comorbid posttraumatic stress disorder. PLoS One 8, e65824.

Paniagua, B., Bompard, L., Cates, J., Whitaker, R., Datar, M., Vachet, C., Styner, M., 2012. Combined SPHARM-PDM and entropy-based particle systems shape analysis framework. SPIE Conference 8317 Progress in Biomedical Optics and Imaging.

Paniagua, B., Lyall, A., Berger, J.B., Vachet, C., Hamer, R.M., Woolson, S., Lin, W., Gilmore, J., Styner, M., 2013. Lateral ventricle morphology analysis via mean latitude axis. Proc. Soc. Photo Opt. Instrum. Eng. 8672.

Petersen, R.C., 2011. Clinical practice. Mild cognitive impairment. N. Engl. J. Med. 364, 2227–2234.

Petersen, R.C., Jack Jr., C.R., 2009. Imaging and biomarkers in early Alzheimer's disease and mild cognitive impairment. Clin. Pharmacol. Ther. 86, 438–441.

Pihlajamaki, M., Jauhiainen, A.M., Soininen, H., 2009. Structural and functional MRI in mild cognitive impairment. Curr. Alzheimer Res. 6, 179–185.

Qiu, A., Brown, T., Fischl, B., Ma, J., Miller, M.I., 2010. Atlas generation for subcortical and ventricular structures with its applications in shape analysis. IEEE Trans. Image Process. 19, 1539–1547.

Reiman, E.M., Jagust, W.J., 2012. Brain imaging in the study of Alzheimer's disease. Neuroimage 61, 505–516.

Reiman, E.M., Uecker, A., Caselli, R.J., Lewis, S., Bandy, D., de Leon, M.J., De Santi, S., Convit, A., Osborne, D., Weaver, A., Thibodeau, S.N., 1998. Hippocampal volumes in cognitively normal persons at genetic risk for Alzheimer's disease. Ann. Neurol. 44, 288–291.

Rey, A., 1964. L'examen clinique en psychologie. Presses Universitaires de France, Paris.

Ridha, B.H., Anderson, V.M., Barnes, J., Boyes, R.G., Price, S.L., Rossor, M.N., Whitwell, J.L., Jenkins, L., Black, R.S., Grundman, M., Fox, N.C., 2008. Volumetric MRI and cognitive measures in Alzheimer disease: comparison of markers of progression. J. Neurol. 255, 567–574.

Roberts, J.S., Karlawish, J.H., Uhlmann, W.R., Petersen, R.C., Green, R.C., 2010. Mild cognitive impairment in clinical care: a survey of American Academy of Neurology members. Neurology 75, 425–431.

Rosen, W.G., Mohs, R.C., Davis, K.L., 1984. A new rating scale for Alzheimer's disease. Am. J. Psychiatry 141, 1356–1364.

Samtani, M.N., Farnum, M., Lobanov, V., Yang, E., Raghavan, N., Dibernardo, A., Narayan, V., 2012. An improved model for disease progression in patients from the Alzheimer's disease neuroimaging initiative. J. Clin. Pharmacol. 52, 629–644.

Schraml, F., Chen, K., Ayutyanont, N., Auttawut, R., Langbaum, J.B., Lee, W., Liu, X., Bandy, D., Reeder, S.Q., Alexander, G.E., Caselli, R.J., Fleisher, A.S., Reiman, E.M., 2013. Association between an Alzheimer's disease-related index and gene dose. PLoS One 8, e67163.

Seo, S., Chung, M.K., Vorperian, H.K., 2010. Heat kernel smoothing using Laplace–Beltrami eigenfunctions. 13th International Conference on Medical Image Computing and Computer Assisted Intervention (MICCAI), pp. 505–512.

Shattuck, D.W., Leahy, R.M., 2002. BrainSuite: an automated cortical surface identification tool. Med. Image Anal. 6, 129–142.

Shi, J., Thompson, P.M., Wang, Y., 2012. Hyperbolic Ricci flow and its application in studying lateral ventricle morphometry. In: Yap, P.-T., Liu, T., Shen, D., Westin, C.-F., Shen, L. (Eds.), Multimodal Brain Image Analysis. Springer, Berlin Heidelberg, pp. 61–76.

Shi, J., Thompson, P.M., Gutman, B., Wang, Y., 2013a. Surface fluid registration of conformal representation: application to detect disease effect and genetic influence on hippocampus. Neuroimage 78, 111–134.

Shi, J., Wang, Y., Ceschin, R., An, X., Lao, Y., Vanderbilt, D., Nelson, M.D., Thompson, P.M., Panigrahy, A., Lepore, N., 2013b. A multivariate surface-based analysis of the putamen in premature newborns: regional differences within the ventral striatum. PLoS One 8, e66736.

Shi, R., Zeng, W., Su, Z., Damasio, H., Lu, Z., Wang, Y., Yau, S.-T., Gu, X., 2013c. Hyperbolic Harmonic Mapping for Constrained Brain Registration. IEEE Conf Comp Vis Patt Recog CVPR '13.

Shi, R., Zeng, W., Su, Z., Wang, Y., Damasio, H., Lu, Z., Yau, S.-T., Gu, X., 2013d. Hyperbolic Harmonic Brain Surface Registration with Curvature-based Landmark Matching. Information Processing in Medical Imaging, 23rd International Conference (IPMI), Asilomar, CA.

Shi, J., Lepore, N., Gutman, B.A., Thompson, P.M., Baxter, L.C., Caselli, R.J., Wang, Y., 2014. Genetic influence of apolipoprotein E4 genotype on hippocampal morphometry: an N = 725 surface-based Alzheimer's disease neuroimaging initiative study. Hum. Brain Mapp. 35 (8), 3903–3918.

Small, G.W., Kepe, V., Ercoli, L.M., Siddarth, P., Bookheimer, S.Y., Miller, K.J., Lavretsky, H., Burggren, A.C., Cole, G.M., Vinters, H.V., Thompson, P.M., Huang, S.C., Satyamurthy, N., Phelps, M.E., Barrio, J.R., 2006. PET of brain amyloid and tau in mild cognitive impairment. N. Engl. J. Med. 355, 2652–2663.

Small, G.W., Siddarth, P., Burggren, A.C., Kepe, V., Ercoli, L.M., Miller, K.J., Lavretsky, H., Thompson, P.M., Cole, G.M., Huang, S.C., Phelps, M.E., Bookheimer, S.Y., Barrio, J.R., 2009. Influence of cognitive status, age, and APOE-4 genetic risk on brain FDDNP positron-emission tomography imaging in persons without dementia. Arch. Gen. Psychiatry 66, 81–87.

Sowell, E.R., Thompson, P.M., Rex, D., Kornsand, D., Tessner, K.D., Jernigan, T.L., Toga, A.W., 2002. Mapping sulcal pattern asymmetry and local cortical surface gray matter distribution in vivo: maturation in perisylvian cortices. Cereb. Cortex 12, 17–26.

Stephenson, K., 2005. Introduction to Circle Packing: The Theory of Discrete Analytic Functions. Cambridge University Press.

Stonnington, C.M., Chu, C., Kloppel, S., Jack Jr., C.R., Ashburner, J., Frackowiak, R.S., 2010. Predicting clinical scores from magnetic resonance scans in Alzheimer's disease. Neuroimage 51, 1405–1413.

Styner, M., Lieberman, J.A., McClure, R.K., Weinberger, D.R., Jones, D.W., Gerig, G., 2005. Morphometric analysis of lateral ventricles in schizophrenia and healthy controls regarding genetic and disease-specific factors. Proc. Natl. Acad. Sci. U. S. A. 102, 4872–4877.

Styner, M., Oguz, I., Xu, S., Brechbühler, C., Pantazis, D., Levitt, J.L., Shenton, M.E., Gerig, G., 2006. Framework for the statistical shape analysis of brain structures using SPHARM-PDM. Insight J. 242–250.

Tae, W.S., Kim, S.S., Lee, K.U., Nam, E.C., Choi, J.W., Park, J.I., 2011. Hippocampal shape deformation in female patients with unremitting major depressive disorder. AJNR Am. J. Neuroradiol. 32, 671–676.

Tang, X., Holland, D., Dale, A.M., Younes, L., Miller, M.I., 2014. Shape abnormalities of subcortical and ventricular structures in mild cognitive impairment and Alzheimer's disease: detecting, quantifying, and predicting. Hum. Brain Mapp. 35 (8), 3701–3725.

Thompson, P.M., Toga, A.W., 2002. A framework for computational anatomy. Comput. Vis. Sci. 5, 1–12.

Thompson, P.M., Giedd, J.N., Woods, R.P., MacDonald, D., Evans, A.C., Toga, A.W., 2000. Growth patterns in the developing human brain detected using continuum-mechanical tensor mapping. Nature 404, 190–193.

Thompson, P.M., Hayashi, K.M., Zubicaray, G.D., Janke, A.L., Rose, S.E., Semple, J., Herman, D., Hong, M.S., Dittmer, S.S., Doddrell, D.M., Toga, A.W., 2003. Dynamics of gray matter loss in Alzheimer's disease. J. Neurosci. 23, 994–1005.

Thompson, P.M., Hayashi, K.M., de Zubicaray, G., Janke, A.L., Rose, S.E., Semple, J., Hong, M.S., Herman, D.H., Gravano, D., Doddrell, D.M., Toga, A.W., 2004a. Mapping hippocampal and ventricular change in Alzheimer's disease. Neuroimage 22, 1754–1766.

Thompson, P.M., Hayashi, K.M., Sowell, E.R., Gogtay, N., Giedd, J.N., Rapoport, J.L., de Zubicaray, G.I., Janke, A.L., Rose, S.E., Semple, J., Doddrell, D.M., Wang, Y., van Erp, T.G.M., Cannon, T.D., Toga, A.W., 2004b. Mapping cortical change in Alzheimer's disease, brain development, and schizophrenia. Neuroimage 23, S2–S18.

Thompson, P.M., Dutton, R.A., Hayashi, K.M., Lu, A., Lee, S.E., Lee, J.Y., Lopez, O.L., Aizenstein, H.J., Toga, A.W., Becker, J.T., 2006. 3D Mapping of ventricular and corpus callosum abnormalities in HIV/AIDS. Neuroimage 31, 12–23.

Thurston, W.P., 1976. Geometry and Topology of Three-Manifolds. Princeton lecture notes.

Toledo, J.B., Cairns, N.J., Da, X., Chen, K., Carter, D., Fleisher, A., Householder, E., Ayutyanont, N., Roontiva, A., Bauer, R.J., Eisen, P., Shaw, L.M., Davatzikos, C., Weiner, M.W., Reiman, E.M., Morris, J.C., Trojanowski, J.Q., 2013. Clinical and multimodal biomarker correlates of ADNI neuropathological findings. Acta Neuropathol. Commun. 1, 65.

Tsui, A., Fenton, D., Vuong, P., Hass, J., Koehl, P., Amenta, N., Coeurjolly, D., DeCarli, C., Carmichael, O., 2013. Globally optimal cortical surface matching with exact landmark correspondence. Proceedings of the 23rd international conference on Information Processing in Medical Imaging. Springer-Verlag, Asilomar, CA, pp. 487–498.

Vemuri, P., Gunter, J.L., Senjem, M.L., Whitwell, J.L., Kantarci, K., Knopman, D.S., Boeve, B.F., Petersen, R.C., Jack Jr., C.R., 2008a. Alzheimer's disease diagnosis in individual subjects using structural MR images: validation studies. Neuroimage 39, 1186–1197.

Vemuri, P., Whitwell, J.L., Kantarci, K., Josephs, K.A., Parisi, J.E., Shiung, M.S., Knopman, D.S., Boeve, B.F., Petersen, R.C., Dickson, D.W., Jack Jr., C.R., 2008b. Antemortem MRI based STructural Abnormality iNDex (STAND)-scores correlate with postmortem Braak neurofibrillary tangle stage. Neuroimage 42, 559–567.

Vemuri, P., Wiste, H.J., Weigand, S.D., Knopman, D.S., Trojanowski, J.Q., Shaw, L.M., Bernstein, M.A., Aisen, P.S., Weiner, M., Petersen, R.C., Jack Jr., C.R., 2010. Serial MRI and CSF biomarkers in normal aging, MCI, and AD. Neurology 75, 143–151.

Wang, Y., Gu, X., Chan, T.F., Thompson, P.M., Yau, S.-T., 2006. Brain surface conformal parameterization with algebraic functions. Med. Image Comput. Comput. Assist. Interv. Proc. II, pp. 946–954.

Wang, Y., Lui, L.M., Gu, X., Hayashi, K.M., Chan, T.F., Toga, A.W., Thompson, P.M., Yau, S.-T., 2007. Brain surface conformal parameterization using riemann surface structure. IEEE Trans. Med. Imaging 26, 853–865.

Wang, Y., Chan, T.F., Toga, A.W., Thompson, P.M., 2009a. Multivariate tensor-based brain anatomical surface morphometry via holomorphic one-forms. Med. Image Comput. Assist. Interv. Proc. 12, 337–344.

Wang, Y., Dai, W., Chou, Y., Gu, X., Chan, T.F., Toga, A.W., Thompson, P.M., 2009b. Studying brain morphology using conformal equivalence class. IEEE 12th International Conference on Computer Vision 2009, ICCV 2009, pp. 2365–2372.

Wang, Y., Dai, W., Gu, X., Chan, T.F., Yau, S.T., Toga, A.W., Thompson, P.M., 2009c. Teichmüller shape space theory and its application to brain morphometry. Med. Image Comput. Comput. Assist. Interv. Proc. 12, 133–140.

Wang, Y., Zhang, J., Chan, T.F., Toga, A.W., Thompson, P.M., 2009d. Brain surface conformal parameterization with holomorphic flow method and its application to HIV/AIDS. Neuroimage 47, 99.

Wang, Y., Zhang, J., Chan, T.F., Toga, A.W., Thompson, P.M., 2009e. Multivariate tensor-based morphometry on surfaces: application to mapping ventricular changes in HIV/AIDS. IEEE International Symposium on Biomedical Imaging: From Nano to Macro (ISBI 2009).

Wang, Y., Zhang, J., Gutman, B., Chan, T.F., Becker, J.T., Aizenstein, H.J., Lopez, O.L., Tamburo, R.J., Toga, A.W., Thompson, P.M., 2010. Multivariate tensor-based morphometry on surfaces: application to mapping ventricular abnormalities in HIV/AIDS. Neuroimage 49, 2141–2157.

Wang, Y., Song, Y., Rajagopalan, P., An, T., Liu, K., Chou, Y.Y., Gutman, B., Toga, A.W., Thompson, P.M., 2011. Surface-based TBM boosts power to detect disease effects on the brain: an N = 804 ADNI study. Neuroimage 56, 1993–2010.

Wang, Y., Shi, J., Yin, X., Gu, X., Chan, T.F., Yau, S.-T., Toga, A.W., Thompson, P.M., 2012. Brain surface conformal parameterization with the Ricci flow. IEEE Trans. Med. Imaging 31, 251–264.

Wang, G., Zhang, X., Su, Q., Chen, J., Wang, L., Ma, Y., Liu, Q., Xu, L., Shi, J., Wang, Y., 2013a. A heat kernel based cortical thickness estimation algorithm. In: Shen, L., Liu, T., Yap, P.-T., Huang, H., Shen, D., Westin, C.-F. (Eds.), Multimodal Brain Image Analysis. Springer International Publishing, pp. 233–245.

Wang, Y., Yuan, L., Shi, J., Greve, A., Ye, J., Toga, A.W., Reiss, A.L., Thompson, P.M., 2013b. Applying tensor-based morphometry to parametric surfaces can improve MRI-based disease diagnosis. Neuroimage 74, 209–230.

Wang, G., Zhang, X., Su, Q., Shi, J., Caselli, R.J., Wang, Y., 2014. A novel cortical thickness estimation method based on volumetric Laplace–Beltrami operator and heat kernel. Med. Image Anal. (Under Review).

Weiner, M.W., Veitch, D.P., Aisen, P.S., Beckett, L.A., Cairns, N.J., Green, R.C., Harvey, D., Jack, C.R., Jagust, W., Liu, E., Morris, J.C., Petersen, R.C., Saykin, A.J., Schmidt, M.E., Shaw, L., Siuciak, J.A., Soares, H., Toga, A.W., Trojanowski, J.Q., 2012. The Alzheimer's Disease Neuroimaging Initiative: a review of papers published since its inception. Alzheimers Dement. 8, S1–S68.

Westman, E., Aguilar, C., Muehlboeck, J.S., Simmons, A., 2013. Regional magnetic resonance imaging measures for multivariate analysis in Alzheimer's disease and mild cognitive impairment. Brain Topogr. 26, 9–23.

Whitwell, J.L., 2009. Voxel-based morphometry: an automated technique for assessing structural changes in the brain. J. Neurosci. 29, 9661–9664.

Whitwell, J.L., Josephs, K.A., Murray, M.E., Kantarci, K., Przybelski, S.A., Weigand, S.D., Vemuri, P., Senjem, M.L., Parisi, J.E., Knopman, D.S., Boeve, B.F., Petersen, R.C., Dickson, D.W., Jack Jr., C.R., 2008. MRI correlates of neurofibrillary tangle pathology at autopsy: a voxel-based morphometry study. Neurology 71, 743–749.

Wolf, H., Jelic, V., Gertz, H.J., Nordberg, A., Julin, P., Wahlund, L.O., 2003. A critical discussion of the role of neuroimaging in mild cognitive impairment. Acta Neurol. Scand. Suppl. 179, 52–76.

Wolz, R., Heckemann, R.A., Aljabar, P., Hajnal, J.V., Hammers, A., Lötjönen, J., Rueckert, D., 2010. Measurement of hippocampal atrophy using 4D graph-cut segmentation: application to ADNI. Neuroimage 52, 109–118.

Yeo, B.T., Sabuncu, M.R., Vercauteren, T., Ayache, N., Fischl, B., Golland, P., 2010. Spherical demons: fast diffeomorphic landmark-free surface registration. IEEE Trans. Med. Imaging 29, 650–668.

Zeng, W., Samaras, D., Gu, X.D., 2010. Ricci flow for 3D shape analysis. IEEE Trans. Pattern Anal. Mach. Intell. 32, 662–677.